J. Phys.: Condens. Matter 5 (1993) 3727–3786. Printed in the UK

REVIEW ARTICLE

Magnetic multilayers: spin configurations, excitations and giant magnetoresistance

R E Camley and R L Stamps
Department of Physics, University of Colorado at Colorado Springs, Colorado Springs, CO 80933-7150, USA

Received 15 February 1993

Abstract. We discuss some of the fundamental properties unique to magnetic multilayers. Complex spin configurations are examined for many different systems and are shown to arise from a simple competition between exchange and Zeeman energies. The spin configurations found in multilayer systems determine macroscopic properties such as the static susceptibility and magnetization, and can lead to anomalous field and temperature behaviour. We also discuss the dynamic behaviour of magnetic multilayers. Emphasis is placed on spin waves in magnetic multilayers with canted spin configurations and the softening of modes at magnetic phase transitions. Furthermore we show that spin wave excitations provide a powerful method for studying exchange interactions and spin configurations. Finally, the phenomenon of giant magnetoresistance in magnetic multilayers, where the resistivity of the metallic structure can be changed by over 60% at room temperature, is discussed. Simple theoretical approaches are used to understand and predict the properties of the multilayer systems and comparisons between theory and experiment are stressed.

Contents

0953-8984/93/233727+60$07.50

1. Introduction

Magnetic multilayers have attracted significant attention recently because of a wide array of fascinating properties. The study of multilayer systems has been motivated by the idea that the properties of multilayer systems can be significantly different from those of any of the components. The reasons for this include:

(1) Interface contributions—since interface effects usually penetrate at least a few layers into the bulk, in thin films the interface may profoundly influence the entire film. Repetition of interfaces as found in a multilayer allows one to prepare a macroscopic bulk sample with properties dominated by the interfaces.

(2) Collective contributions—the layered structure itself can allow new static configurations and new dynamic modes. In the case of a periodic multilayered system, a superlattice, the new periodicity introduces band gaps in the dispersion relations for the fundamental excitations in the structure. As usual, these gaps play a significant role in establishing the properties of the material.

(3) The properties of the multilayer may be tailored—the multilayer structure is synthetically prepared. High-quality multilayers are fabricated with the thicknesses of the different materials varying from about 10 Å to 200 Å. By varying the microscopic structure, i.e. the layering pattern, the macroscopic properties can be altered to meet desired characteristics.

Let us now examine these ideas in a little more detail, and in particular how these ideas are reflected in a magnetic multilayer. In figure 1 we show a schematic diagram for a simple magnetic superlattice consisting of alternating films of different magnetic materials. Because of the layered structure the magnetic moments (magnitude and orientation) can vary significantly from layer to layer.

At the interfaces, everything can be and, in fact, is likely to be different. For example, the interface exchange constant can have a different sign from the exchange in the bulk of either magnetic material. This occurs in Fe/Gd and Co/Gd multilayer systems [1, 2] where Gd, Fe and Co are all ferromagnets, but the coupling across the Fe/Gd or Co/Gd interface is antiferromagnetic [3, 4]. The spin magnitudes for atoms at the interfaces can be quite different from those in the bulk and may be either enhanced or reduced. Anisotropy fields which in the bulk direct the spins parallel to the layers might at the interface direct the spins perpendicular to the layers [5, 6].

In terms of collective features in equilibrium structures, one of the most interesting magnetic examples is found in systems that have magnetic unit cells which are larger than the chemical unit cells. A representative case here is found in Gd/Y superlattices [7, 8]. Although Y is non-magnetic, there is an effective antiferromagnetic interaction between blocks of Gd spins for certain thicknesses of intervening Y layers. With no applied field,

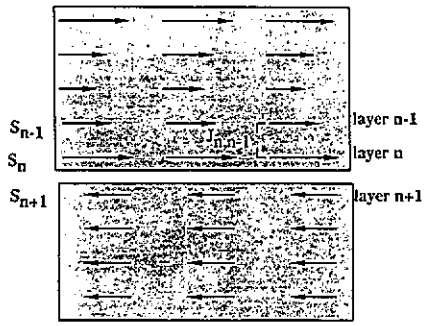

Figure 1. A schematic diagram for the unit cell of a simple magnetic superlattice consisting of alternating films of different magnetic materials. We deal with structures where all the spins in a layer are identical, but the magnitude of the spin S_n, in layer n, and its orientation may change from layer to layer. The exchange coupling between two layers is also shown schematically.

neighbouring Gd films have oppositely directed spins, i.e. we have something similar to a macroscopic antiferromagnet. If a magnetic field is applied parallel to the layers, the system goes essentially into the macroscopic equivalent of the antiferromagnetic spin-flop state. Here the spins in one Gd film are in plane but canted away from the applied field. In a neighbouring film the Gd spins are canted in the other direction. The magnetic repeat distance in either case is two chemical unit cells.

Collective features are also seen in the magnetic excitations [9–11]. Even in layered magnetic-non-magnetic systems one may have a collective excitation of the system because the magnetic films interact via long-range dipolar fields. Of course in magnetic/magnetic structures the spins interact via both the short-range exchange interactions and the dipolar fields.

Magnetic materials are used in a variety of applications, including magnetoresistive heads and magnetic or magneto-optical recording. For these applications it is desirable to be able to adjust or tune features of the magnetic materials in order to achieve optimum results. Magnetic properties which can be altered by changing the layering pattern include coercive fields, saturation magnetization, magnetization as a function of temperature, static and dynamic susceptibility, and compensation points.

In the next three sections, we present a brief review of some of the properties of magnetic multilayers. We stress simple theoretical approaches which are useful in understanding and predicting the properties of magnetic multilayers. Details of growth techniques and experimental characterization of magnetic multilayers can be found in a number of excellent review articles [12, 13]. In section 2 we concentrate on the equilibrium structures for magnetic superlattices and how the experimental results can be understood with a simple mean-field model. Section 3 is devoted to a discussion of magnetic excitations in superlattices, while section 4 discusses an exciting surprise in magnetic multilayers—the phenomena of giant magnetoresistance. Finally there are some concluding remarks in section 5.

2. Equilibrium spin configurations

By now many different layered structures of magnetic and non-magnetic materials have been fabricated. Examples (meant to be illustrative rather than exhaustive) of these include multilayers constructed by alternating layers of:

(1) ferromagnets with
non-magnets—Ni/Mo [10, 14], Fe/Si [15], Gd/Y [7, 8], Co/Ru [16]
ferromagnets (ferromagnetic interfacial coupling)—Fe/Ni [17]

ferromagnets (antiferromagnetic interfacial coupling)—Fe/Gd [18–24], Co/Gd [2]
helimagnets—Gd/Dy [25, 26]
antiferromagnets—Fe/Cr [27]

(2) helical or conical with non-magnets—Dy/Y [28], Ho/Y [13], Er/Y [29];

(3) antiferromagnets with antiferromagnets—FeF_2/CoF_2 [30] and Fe_3O_4/NiO [31].

These classifications can be somewhat misleading. For example bulk Y is non-magnetic, but, as mentioned earlier, when sandwiched between Gd or Dy films, Y mediates an effective exchange interaction between the magnetically ordered films. Similarly, bulk Cr is antiferromagnetic (technically one has a spin density wave in Cr but the antiferromagnetic structure is stabilized with the addition of a few impurities); however, this does not appear to play a fundamental role in the Fe/Cr superlattices.

The variety of magnetic materials used as building blocks in the multilayers has led to an enormous range of resulting magnetic behaviour. Essentially these structures form a new class of magnetic materials with properties significantly different from their constituents. The basis for most of these new properties is the magnetic structure of the multilayer. Thus is this section we explore a simple theoretical technique for determining equilibrium spin configurations. This technique is then applied to some of the more interesting magnetic multilayer structures. In particular, we discuss bulk structures of Gd/Y, Fe/Gd and Gd/Dy for which both theoretical and experimental results are available. We also look at changes in these structures which appear in finite superlattices due to surface effects.

2.1. Theoretical development

The equilibrium spin structure is, of course, determined by the condition that the free energy should be a minimum. In principle there could be many contributions to the total free energy coming from, for example, the exchange energy, the Zeeman energy of the spins in an external field, magnetoelastic energy, and anisotropy energy. Thus the Hamiltonian for the system is of the form

$$H = H_{\text{ex}} + H_{\text{Zeeman}} + H_{\text{ME}} + H_{\text{anis}} \tag{1}$$

where

$$H_{\text{ex}} = \frac{1}{2}\sum_{i,j} J_{ij} \boldsymbol{S}_i \cdot \boldsymbol{S}_j \tag{2}$$

is the exchange energy; H_{ME} is the magnetoelastic energy and H_{anis} is the anisotropy energy. Finally, the energy of the individual spins in the presence of a magnetic field is given by

$$H_{\text{Zeeman}} = -g\mu_{\text{B}} \sum_i \boldsymbol{S}_i \cdot \boldsymbol{H}_0. \tag{3}$$

Here the sums involve the spins at sites i and j. In the systems to be considered throughout we will assume that all spins within an atomic layer lie in the plane of the layer and all point in the same direction. As we will see explicitly below this allows a treatment where one layer interacts with another in contrast to sums over all individual spins.

Simple considerations about how these various terms change as the number of layers in a unit cell is changed allow us to understand one reason for the great adjustability of the magnetic multilayer structure. As an example, the interface exchange energy is

essentially independent of the number of layers of spins within each film. In contrast the Zeeman energy ought to scale nearly linearly with the number of layers of spins. As a result, in thin films interface exchange energy plays a dominant role in determining the equilibrium structure while for thicker films the Zeeman energy is also significant. This competition between interface exchange energy and Zeeman energy can lead to a variety of unique phase transitions between different equilibrium structures which are quite sensitive to external applied fields.

Clearly the Hamiltonian of equation (1) can be quite challenging. We review here a simpler model which has been used to study equilibrium structures and explain magnetization data in several superlattices [32–39]. We neglect anisotropy and magnetoelastic energies and study a Hamiltonian with an effective exchange coupling between spins in different layers. In this case the Hamiltonian can be written

$$H = \sum_{\text{layer } n} \sum_{m=0,\pm1,\pm2} \frac{1}{2} J_{nm} \boldsymbol{S}_n \cdot \boldsymbol{S}_{n+m} - \sum_{\text{layer } n} g_n \mu_B \boldsymbol{H}_0 \cdot \boldsymbol{S}_n \tag{4}$$

where J_{nm} is the effective interlayer coupling between spins in layers n and $n+m$ and g_n is the effective Landé g factor for the spins S_n in layer n. Here S_n represents all the spins in a layer since they are presumed parallel. Also in this expression we explicitly have an exchange interaction between spins in the same layer ($m = 0$), and spins in next ($m = \pm1$) and next-nearest ($m = \pm2$) layers. A number of potential complications exist even in this simplified Hamiltonian. For instance the Hamiltonian needs to be modified if the two materials have different densities or different crystal structures. However we neglect these effects in our simple treatment.

The above Hamiltonian can be solved, approximately, by several methods. One can convert the problem into a continuous system [33, 40–42] and obtain analytic solutions in the $T = 0$ limit where one can assume a constant amplitude for the magnetic moments. However such an approximation breaks down at higher temperatures and when the structure changes rapidly from layer to layer. A different, more general, method for finding the ground state of the above Hamiltonian is the iterative energy minimization scheme described below.

We first describe the iterative energy minimization method for the $T = 0$ case. One starts with an assumed set of values for the angular position of each layer of spins. In many cases the spins will lie in a plane parallel to the interfaces (this reduces the demagnetization energy) and for simplicity we will use this assumption. It is also assumed that all spins in each layer are equivalent. Due to exchange coupling, the energy of the spins in any given layer depends on the orientation and magnitude of the spins in the nearby layers. An arbitrary layer n, of spins, can be regarded as having an energy E_n where

$$E_n = \sum_{m=0,\pm1,\pm2} J_{nm} \boldsymbol{S}_n \cdot \boldsymbol{S}_{n+m} - g_n \mu_B \boldsymbol{H}_0 \cdot \boldsymbol{S}_n \tag{5}$$

or in terms of the angle θ_n that the spins in layer n make with the applied field

$$E_n = \sum_{m=0,\pm1,\pm2} J_{nm} S_n S_{n+m} \cos(\theta_n - \theta_{n+m}) - g_n \mu_B S_n H_0 \cos(\theta_n). \tag{6}$$

Thus at $T = 0$ a single variable for each layer, θ_n, characterizes the magnetic structure. This energy is minimized by choosing the angle θ_n generated by the minimization condition

$$\partial E_n / \partial \theta_n = 0. \tag{7}$$

This procedure can be viewed as rotating the spins in the nth layer to lie parallel to their effective field, a process which reduces the layer's energy. We can then find a configuration as follows: a different layer is then randomly chosen and the spins in that layer are rotated to lie in the direction of the local effective field. The process is continued until one has a self-consistent, stable state where all the spins are aligned with the effective fields produced by the neighbouring spins. Since the method only minimizes the energy locally, different initial configurations may lead to different self-consistent final states. The ground state is, of course, the stable state with the lowest energy for the entire structure.

At finite temperatures, both the direction and thermal averaged magnitude of the spins in each layer must be specified. In this case the iteration procedure is slightly different. A layer of spins is first rotated into the direction of the effective field, and then the spin's thermal averaged magnitude in that direction is found through the use of the Brillouin function

$$\langle S_n \rangle = S_n B_{S_n}(x) \tag{8}$$

where

$$x = g_n \mu_B S_n H_n / kT. \tag{9}$$

The Brillouin factor is given by

$$B_S(x) = [(2S+1)/2S] \coth[(2S+1)x/2S] - (1/2S) \coth(x/2S). \tag{10}$$

Here $\langle S_n \rangle$ is the thermal average of the spins in the nth layer in the direction of the effective field. H_n is the effective field acting on layer n. The effective field is now given by

$$\boldsymbol{H}_n = \boldsymbol{H}_0 + \sum_{m=0,\pm1,\pm2} \frac{J_{nm}}{g_n \mu_B} \langle \boldsymbol{S}_{n+m} \rangle. \tag{11}$$

Note that in the effective field the spins in the neighbouring layers are replaced by their thermal averaged magnitudes. Again the entire operation is iterated through all spins until a self-consistent state emerges.

Now the ground state is the one with the lowest free energy. At $T = 0$ the energy is *not* simply given by summing over the individual layer energies, i.e.

$$E_{\text{total}} \neq \sum_n g_n \mu_B \boldsymbol{S}_n \cdot \boldsymbol{H}_n \tag{12}$$

since this counts the exchange energy twice. Similarly, for $T \neq 0$ one must be careful in evaluating the free energy to avoid counting the average exchange energy twice. In the mean-field approximation the partition function for the spins in layer n is given by

$$Z_n = \left\{ \sinh\left[(2S_n + 1) g_n \mu_B H_n / 2kT \right] \right\} \Big/ \sinh\left[g_n \mu_B H_n / 2kT \right]. \tag{13}$$

The total partition function is then

$$Z = \prod_n Z_n. \tag{14}$$

Finally, the free energy for the entire structure is given by [43]

$$F = -kT \sum_n \ln Z_n - \frac{1}{2} \sum g_n \mu_B \langle S_n \rangle H_{ex} \tag{15}$$

where the second term on the right eliminates the 'double counting' of the average exchange energy.

In practice the iteration procedure requires of the order of 1000–100 000 iterations per layer to reach a converged state. It generally takes a larger number of iterations to find a converged state near a phase transition. Of course, the final state may only be a local minimum and it is not guaranteed that the true ground state will always be found by this method. Nonetheless, if one takes a sufficient number of different initial sets of angles, the method seems to discover all the low-energy stable states.

We note in passing that this mean-field theory is really the simplest possible approximation that takes into account a layer-by-layer variation spin orientation and thermal averaged magnitude. Such methods have been used previously in thin-film calculations [44]. Improvements would include Bethe–Peirels–Weiss methods or Monte Carlo techniques. However these methods involve significantly larger computational investment.

2.2. Comparison of theoretical and experimental results for bulk superlattices

Among the most interesting of the magnetic superlattice structures are those which involve some antiferromagnetic coupling. In this case the exchange energy favours some kind of antiparallel alignment while the Zeeman energy due to an external field favours a ferromagnetic-like arrangement. As a result, these structures can display a fascinating set of phase transitions, with the transition temperatures and fields controlled by changing the layering pattern. We therefore concentrate on superlattices with antiferromagnetic coupling.

One of the 'simplest' layered systems with an interesting magnetic structure and a fascinating dependence on layering pattern is the Gd/Y superlattice. Although bulk Y is normally non-magnetic, in the Gd/Y superlattice the Y layers mediate an effective exchange interaction between neighbouring Gd films. Yafet and co-workers [45, 46] has shown that this is essentially due to the RKKY interaction. The RKKY interaction is often invoked for discussions of magnetic impurities in a non-magnetic host. In this case, one magnetic impurity produces a spin polarized electron cloud around itself. This spin polarized electron cloud can then interact with a second magnetic centre to produce a long-range exchange interaction which depends on the distance R between the two magnetic impurities. For large R and a free electron gas, the RKKY exchange has the functional form

$$J(R) \simeq A\left[\sin\left(2k_F R\right)\right]/\left(2k_F R\right)^3 \tag{16}$$

where k_F is the Fermi wavevector. The key point here is that the exchange interaction is *oscillatory*, depending on the *distance* between impurity spins. For metals the oscillation period is relatively short, of the order of a few Å. Instead of just considering two impurity spins, Yafet considered two planes of impurity spins and showed that the exchange interaction was still oscillatory. In this case the coupling depends on the distance z between planes and has the form

$$J(z) \simeq B\left[\sin\left(2k_F z\right)\right]/z^2. \tag{17}$$

Clearly, the exchange still oscillates as a function of distance and the expected oscillation period is still only a few Å.

The oscillatory behaviour of the exchange as a function of spacer film thickness in Gd/Y superlattices was beautifully demonstrated in experiments by Kwo *et al* [7]. Figure 2 shows magnetization as a function of Y thickness for a series of Gd/Y samples. The large values of magnetization occur for Y thicknesses where the coupling between Gd films is

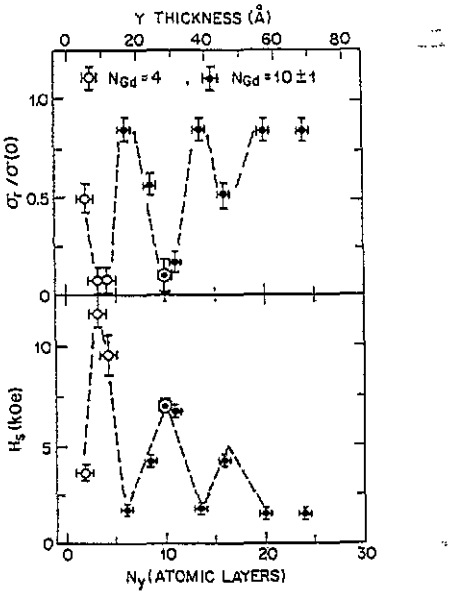

Figure 2. Experimental results on Gd/Y multilayers showing alternation of the zero-field magnetization (top) and the field required for saturation (bottom) as a function of thickness of Y. Low magnetizations and high saturation fields indicate antiferromagnetic coupling. (After [7]).

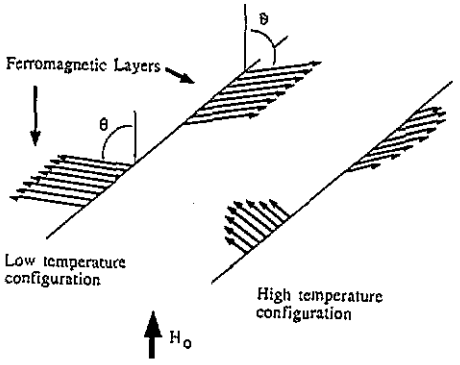

Figure 3. Schematic spin flop of Gd/Y- or Fe/Cr-type structure. The spins in neighbouring films attempt to be antiparallel to each other but are canted in the direction of the applied field. In the high-temperature configuration the thermal averaged magnitude of the spins is lower at the edges of the ferromagnetic films. This results in a smaller canting angle θ for the same applied field.

ferromagnetic, and when the coupling is antiferromagnetic the magnetization is nearly zero, indicating that the Gd spins in neighbouring films are antiparallel.

Recently a series [47] of ferromagnetic/non-magnetic (Fe/Cr [27], Co/Ru [16], Co/Cu [48]) structures has been studied, where the non-magnetic space layers mediate an effective exchange between the magnetic layers. These structures were fabricated by a number of different methods including MBE and sputtering. As in the case of Gd/Y the exchange is ferromagnetic or antiferromagnetic depending on the thickness of the spacer film. However in this case the oscillation length is typically of the order of 10–12 Å, with some periods as large as 18–20 Å. Much shorter-range oscillations (2–3 Å) have also been observed in carefully prepared samples. Despite the differences in the length scale, coupling in these systems has also been attributed, at least in part, to RKKY-type interactions. A detailed discussion of the origin of the coupling is beyond the scope of this paper [49–53].

When ferromagnetic films are antiferromagnetically coupled, through a spacer layer for example, application of a magnetic field produces some interesting results. Because of the competition of interface exchange and Zeeman energies [7, 8], the ground state is not a macroscopic antiferromagnetic state where the ferromagnetic films are strictly antiparallel. Instead the equilibrium structure resembles a macroscopic spin-flop state which represents a compromise between exchange and Zeeman energies. The resulting configuration is illustrated in figure 3. An increase in the external field reduces the canting angle θ and changes the net magnetic moment of the structure. The magnetization is thus very sensitive to applied fields and also to temperature, which plays a strong role in determining the

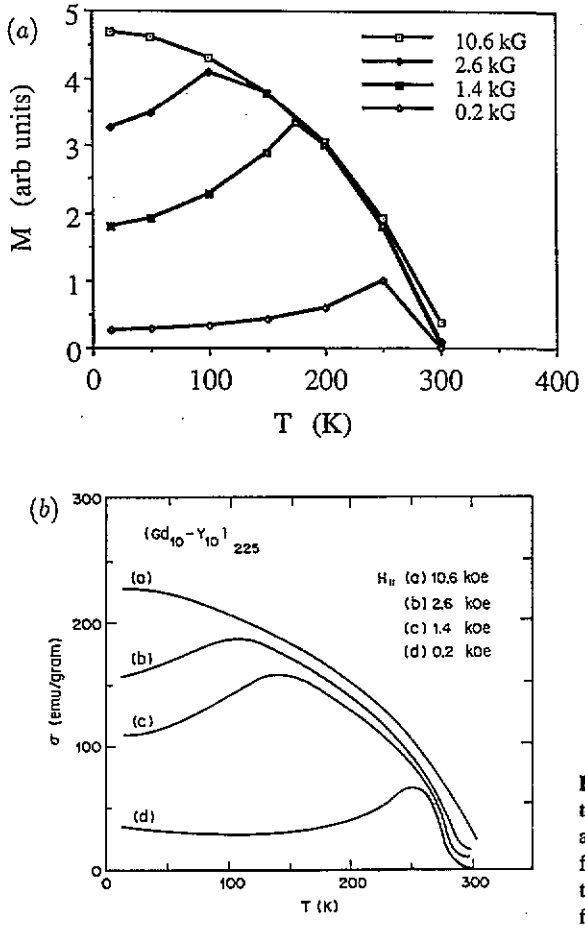

Figure 4. Magnetization as a function of temperature for Gd/Y superlattices: (*a*) theory and (*b*) experiment. Experimental results are from [7]. The increase in magnetization as temperature increases is shown schematically in figure 3.

average interlayer exchange energy.

In figure 4 we present theoretical and experimental results for the magnetization as a function of temperature for Gd/Y superlattices [54]. We see an unusual temperature dependence with a magnetization that *increases* as temperature is increased. This can be readily understood by looking at the exchange coupling of the Gd spins. The Gd spins on the interior are strongly coupled to each other compared to those on the exterior which are only weakly coupled on the Y side via the RKKY interaction. When the temperature is increased, the Gd spins in the interior thus retain a larger thermal averaged magnitude than those on the exterior since they see a larger effective field. As a result, the interface exchange energy (which should scale as $J_i\langle S_{\mathrm{Gd-exterior}}\rangle^2$) is rapidly reduced and the competition between exchange and Zeeman energies now favours a state where the Gd moments point more closely along the external field. This is automatically included in the iterative calculation and the result are illustrated schematically in figure 3. Thus even though $\langle S_{\mathrm{Gd}}\rangle$ decreases as the temperature increases, the change in orientation of the Gd spins is sufficiently large that the magnetization increases. As T continues to increase the $\langle S_{\mathrm{Gd}}\rangle$ begin to decrease very quickly and the magnetization decreases (more or less as single Gd films). The field dependence of the magnetization is also striking. Here we have an *ordered* state which displays a significant change in magnetization as a function of field.

Several other systems have been investigated both experimentally and theoretically. One such system is composed of alternating ferromagnetic films which couple antiferromagnetically at the interfaces (i.e. Fe/Gd or Co/Gd). Such antiferromagnetic coupling is a reasonably general feature of transition metal/rare earth systems. There are three important phases in the Fe/Gd system [33]:

(1) The Gd-aligned phase—the structure here has Gd fully aligned with the applied field and the Fe spins antiparallel to the field. This phase occurs when the net thermal magnetic moment in the Gd films is much larger than that in the Fe films.

(2) The Fe-aligned phase—here the Fe spins are aligned with the field and the Gd spins are oppositely oriented. This phase occurs when the net magnetic moment in the Fe films is larger than that in the Gd films.

(3) The twisted (or canted) phase—here the spins in each layer make a different angle with respect to the applied field. In this phase, the spin configuration can vary from something similar to the spin-flop phase in an antiferromagnet to a configuration similar to that in a domain wall. This phase occurs typically when the net magnetic moments in the Fe and Gd films are close to each other. The phases are illustrated in figure 5.

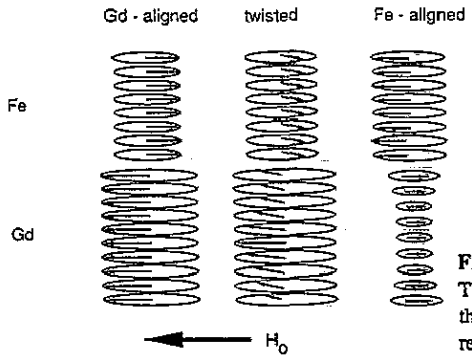

Figure 5. Schematic illustration of phases of Fe/Gd structure. The Fe-aligned state often occurs at higher temperatures where the thermal averaged magnitude of the Gd is significantly reduced.

As we have seen, the different phases arise from a competition between Zeeman and exchange energy. For small magnetic fields the Zeeman energy is less important and the exchange energy generally favours the aligned states. Clearly the films with the larger moment will align parallel to the field. This introduces a strong temperature dependence since the thermal averaged magnetic moment in Gd changes rapidly compared to that of Fe since the Gd spins see a smaller effective field. For moderate fields both exchange and Zeeman energy are important. This favours the twisted state. Changes in the layering pattern can make significant changes in the field–temperature (h–t) phase diagram since the balance between exchange and Zeeman energies depends critically on relative thickness. In figures 6 and 7 we present theoretical phase diagrams for a Fe/Gd superlattice with a unit cell of 13 Fe/5 Gd and a second diagram for a system with a unit cell of 14 Fe/4 Gd. We see that the addition of just one layer produces a dramatic shift in equilibrium properties.

The microscopic phases are reflected in such macroscopic measurements as magnetization as a function of temperature and static susceptibility. In particular the twisted phase displays a very large susceptibility. The reason for this is clear. Susceptibility measures the ability of the spin configuration to change due to an external field. In the aligned state only the magnitudes can change. In the twisted state both the magnitudes and the orientations of the spin can change and this leads to a significantly enhanced susceptibility. Note also

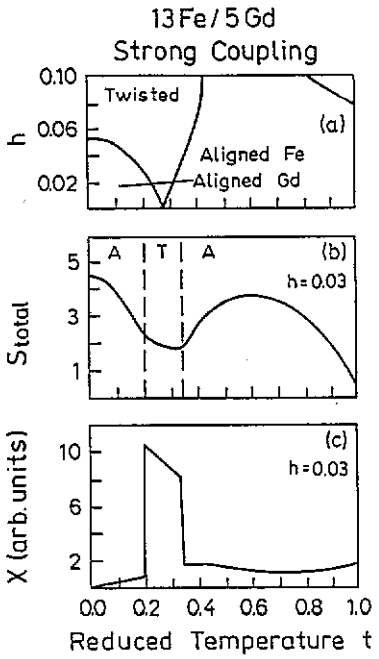

Figure 6. Magnetic properties of a 13 layers Fe/5 layers Gd multilayer: (*a*) phase diagram; (*b*) net magnetic moment; (*c*) static susceptibility at a given external field. t is the reduced temperature given by T/T_{c-Gd} and h is the reduced field given as a fraction of the exchange field. (After [34].)

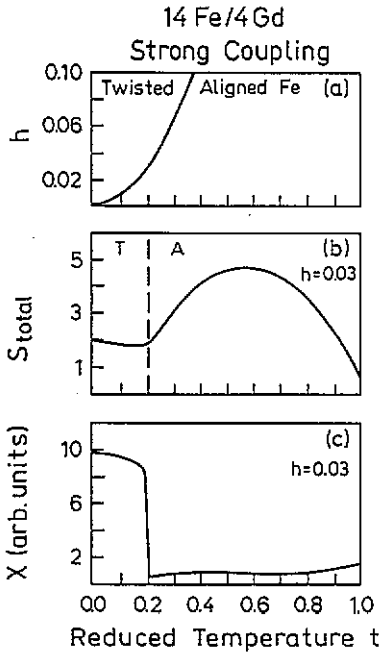

Figure 7. Magnetic properties of a 14 layers Fe/4 layers Gd multilayer: (*a*) phase diagram; (*b*) net magnetic moment; (*c*) static susceptibility at a given external field. t is the reduced temperature and h is the reduced field as in figure 6. Note significant changes in the results as compared to the structure shown in figure 6. (After [34].)

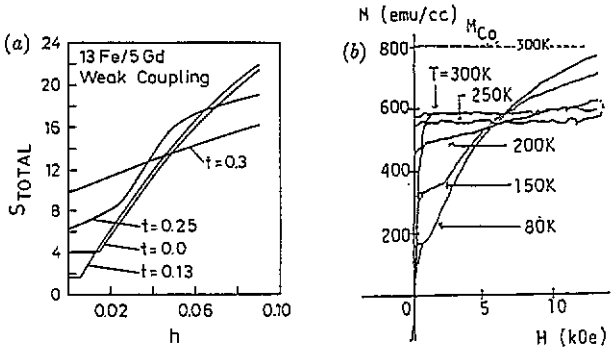

Figure 8. Magnetization as a function of applied field for (*a*) Fe/Gd superlattice (theory) and (*b*) Co/Gd superlattice (experiment). In the theoretical plot t is the reduced temperature and h is the reduced magnetic field as in figure 6. (Theory after [34] and experiment after [2].)

that the behaviour of the net moment as function of temperature is very different for the two samples.

In figure 8 we compare theoretical results [34] for M versus applied field for an Fe/Gd superlattice with experimental results for a Co/Gd superlattice [2]. (The Co/Gd superlattice

has essentially the same physics as the Fe/Gd structure.) We see good qualitative agreement between the experiment and theory and can clearly distinguish phase changes from aligned states (S_{total} nearly constant) to twisted states (S changing rapidly with field).

Theoretical results for the magnetic phase diagram of the Fe/Gd system were presented in [33 and 34]. In addition it was shown that the critical field necessary to cause a transition from the Gd-aligned phase to the twisted phase at a fixed temperature decreased significantly as the thickness of the Gd layer was increased. Recently systematic experimental explorations of the Fe/Gd system have been initiated by several different groups [18–24, 55, 56]. These studies have confirmed the magnetic phase diagram (as can be seen in figure 9) and the dependence of the critical field on the thickness of the layers, and have verified that the susceptibility is largest in the twisted state. An interesting feature which emerges from these studies, some of which made direct comparisons between experiment and theory, is that the Gd films in the superlattices behave as if their magnetizations are reduced by 20–25% from bulk Gd. The reason for this is not yet known.

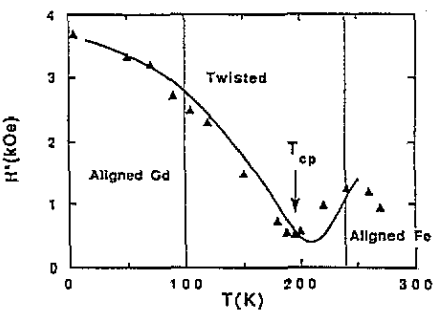

Figure 9. A comparison of experiment (▲) and theory (full curve) for the magnetic phase diagram of Fe/Gd. The calculation used a value for the Gd magnetization which was reduced by about 20% from that of bulk Gd. (After [56].)

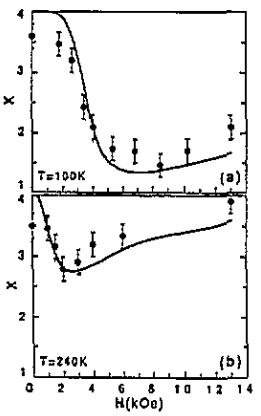

Figure 10. Experimental (filled circles) and theoretical (full curves) Mössbauer results for Fe/Gd. X is the ratio of the intensities of two Mössbauer lines seen in the typical sextuplet spectrum for Fe. In a 45° geometry X can be related to the angle that the Fe spins make with the external field. $X = 4$ indicates that the Fe spins are either parallel or antiparallel to the applied field. $X = 1.33$ indicates the Fe spins are perpendicular to the applied field. The temperatures correspond to the vertical lines in figure 9. (After [56].)

An experimental group in France used a clever variation of Mössbauer spectroscopy to obtain the microscopic orientation of the Fe spins with respect to the external field [24]. In a typical Mössbauer spectrum for BCC Fe one sees six peaks. These peaks occur with relative intensities $3{:}X{:}1{:}1{:}X{:}3$. The factor X depends on the angle between the γ-ray direction and the direction of the magnetization in Fe. Using a 45° incident geometry, X may be related to the angle between the Fe moments and the applied field. One can show that in this geometry $X = 4$ indicates that the Fe moments are either parallel or antiparallel to the applied field. At $X = 1.33$ Fe is perpendicular to the applied field. A comparison of experimental and theoretical results for X as a function of magnetic field has recently been reported for an Fe(42 Å)/Gd(84 Å) superlattice and typical results are shown in figure 10.

Here for T = 100 K and at low field one sees that $X \simeq 4$ indicating that the Fe moments are antiparallel to the applied field. As the field is increased the phase transition to the twisted state occurs around H = 2.5 kG and the Fe moments begin to turn toward the direction of the applied field. At H = 8.5 kG X = 1.45 and the Fe moments are practically perpendicular to the field. The behaviour at T = 240 K is significantly different. In this case X is generally near four and the Fe moments are nearly aligned with the external field over the entire range of applied field. The agreement between theory and experiment is quite good indicating that this system is reasonably well understood.

We describe one final bulk system, a Gd/Dy superlattice, in detail. Bulk Dy is a very interesting material which develops a helical magnetic order below 178 K [57]. A second phase transition occurs in bulk Dy at around 85 K when the magnetic ordering changes to a ferromagnetic state. In thin films the phase transition to the ferromagnetic state is suppressed [28, 29]. As might be expected, the Dy behaviour in the superlattice structure is also significantly altered from its behaviour in the bulk.

In figure 11 we show the experimental $M(T)$ curves for four different superlattice structures. Here we see that as the temperature is lowered, the Gd slabs first become ferromagnetically ordered at T_c. The values of T_c are slightly depressed compared to bulk Gd where T_c = 292 K. We find T_c = 250 K for superlattices with five Gd layers in a unit cell and T_c = 290 K for superlattices with ten Gd layers in a unit cell. This decrease is due to finite-size effects and is in good agreement with earlier results. Upon further reduction of temperature a local maximum in $M(T)$ occurs followed by a minimum, which occurs at a temperature between 100 K and 200 K depending on the specific superlattice bilayer period. Finally, $M(T)$ increases as the temperature is lowered toward 10 K. Since bulk Dy develops a helical order at T_N = 178 K, the minimum followed by the sharp rise of $M(T)$ in the Gd/Dy superlattices is undoubtedly a consequence of the complex spin structures of the Dy slabs and the Gd slabs. We note that for the 5 Gd/5 Dy and 10 Gd/5 Dy samples, one recovers a very large fraction of $M_s(0)$ with a field of only 0.1 kOe at 10 K, and thus the spin structure must be very nearly ferromagnetic. However in the 5 Gd/10 Dy and 10 Gd/10 Dy samples, where the thickness of the Dy slabs is doubled, the magnetization at 0.1 kOe is significantly less than $M_s(0)$. Neutron scattering results [26] at 80 K confirm this picture. For the 5 Gd/5 Dy and 10 Gd/5 Dy samples one sees a primary magnetic periodicity of the chemical unit cell. This is consistent with a ferromagnetic state. For the 5 Gd/10 Dy and 10 Gd/10 Dy samples, one sees a primary periodicity associated with a doubled magnetic unit cell. In every case there is a doubled unit cell at the minimum in the magnetization. This is consistent with an alternating helical state where the doubled unit cell contains Dy films which show opposite helicities in their magnetic structure. The alternating helicity state is described in more detail later.

In order to describe the helical ordering in Dy, one must include both nearest-layer and next-nearest-layer exchange interactions, A_1 and A_2 respectively [57]. As is well known the turn angle Φ of a bulk helical structure is given by the equation $\cos \Phi = A_1/(-4A_2)$. In both bulk Dy and Dy films, this turn angle varies with temperature. As is common, we assume that this variation can be described by a temperature-dependent value for A_2 [57]. The resulting turn angles are remarkably close (within a few percent) to the bulk values for temperatures above the bulk phase transition [58]. Earlier work has shown that the bulk phase transition to a ferromagnetic state is suppressed in thin Dy films, and our assumptions for the superlattice values are consistent with this. The assumed values for the turn angle as a function of temperature are shown in figure 12 along with the values known for bulk Dy samples. The same variation of A_2 with temperature is used for all four structures considered here.

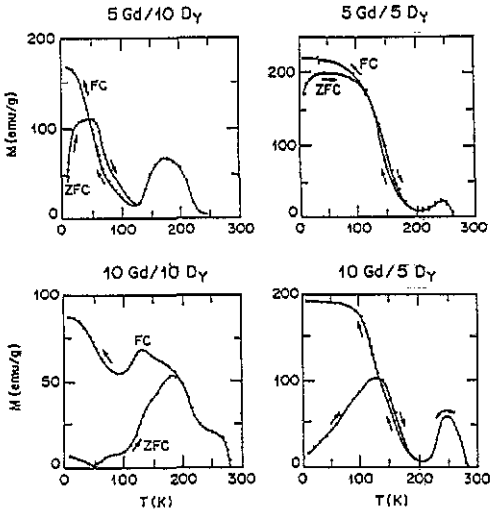

Figure 11. Magnetization as a function of temperature for Gd_n/Dy_m superlattices. ZFC indicates the results for the zero-field-cooled process while FC means field cooled. (After [25].)

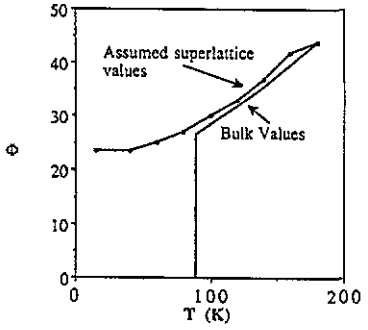

Figure 12. Turn angle in Dy as a function of temperature for bulk Dy compared to values used in the theoretical calculations.

For simplicity, anisotropy is neglected. This probably results in some differences between theory and experiment, particularly in the details of the magnetic structure. For example this might cause the structure to be asymmetric about the applied field as discussed earlier in superlattices with antiferromagnets [39]. However, as we will see, all the major features of the magnetization curves seem to be reproduced properly, so this is probably not too severe an approximation.

The mean-field iterative method described above is used to find the ground state structure for this system. Depending on the initial set of angles chosen, a variety of final stable states can emerge. These include a ferromagnetic phase where all spins line up along the external field, an alternating-helical phase (if the helicity is positive in one Dy film it is negative in the next Dy film), a fan phase and an 'antiferromagnetic phase'. Typical structures for some of these phases are illustrated in figure 13.

The alternating-helicity state is particularly interesting in that the magnetic unit cell is twice the length of the chemical unit cell. This alternation of helicity generally allows the Gd spins to lie near the direction of the applied field. In contrast, a continuous-helicity state, where the helicity in each Dy film has the same sign, would result in Gd spins, on average, having no particular orientation with respect to the field. Thus the alternating-helicity state produces a significant gain in Zeeman energy. Since the helicity within a single Dy film is maintained there is also not much cost in exchange energy. This is in contrast to a fan phase where the helicity *within* a film is reversed. The existence of the alternating-helicity state is a dramatic example of a collective superlattice effect.

The theoretical results for $M(T)$ are presented in figure 14. The comparison between experiment and theory is really quite good with a slight exception for the 10/10 structure. We see from the theoretical magnetization results that the alternating-helicity phase plays a very important role. As the temperature increases the magnetization in this phase first shows a rapid decrease and then an increase. This reflects, in part, the change in turn angle as a function of temperature. At the minimum in the magnetization the Gd spins in

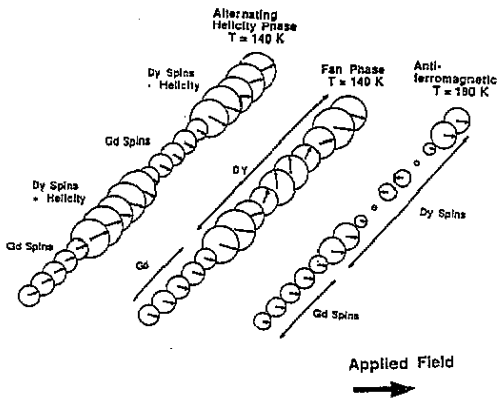

Figure 13. Illustration of the alternating-helicity phase, the fan phase and the antiferromagnetic phase in Gd/Dy superlattices. (After [25].)

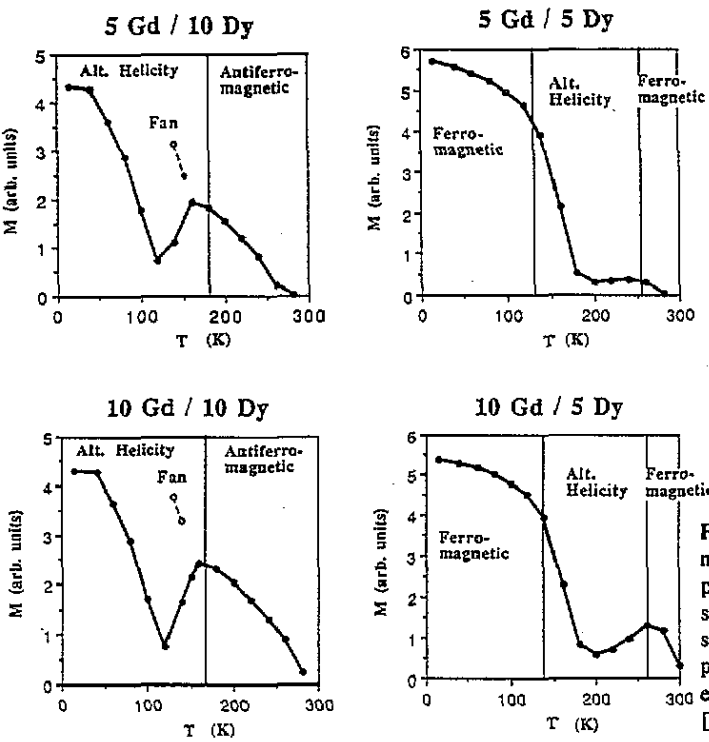

Figure 14. Theoretical results for magnetization as a function of temperature for Gd/Dy superlattices as shown in figure 11. The solid lines show the ground state. The fan phase, where shown, is stable but exists at a higher energy. (After [25].)

neighbouring films are nearly antiparallel to each other. By changing the number of Dy layers one also changes the net angle between the Gd spins in neighbouring layers and as a result the minimum in $M(T)$ occurs at a different temperature. Here we see that the minimum is shifted by about 100 K by changing the number of Dy layers from five to ten.

2.3. Surface phase transition

We now turn to the influence of the outermost surfaces of the magnetic structure of a finite superlattice. The surface layer plays a special role in the magnetic structure simply because

it is exchange coupled to other spins on only one side. Thus in the competition between exchange and Zeeman energies, the influence of the exchange energy is reduced and it is easier for an external field to direct the surface spins. As the outermost layer of spins tries to turn toward the field direction, the remaining layers must adjust their orientations as well. These surface-induced phase transitions can occur at magnetic field strengths well below that required for the equivalent bulk phase transition [59, 60]. Also the reconstructed state can have surprisingly large penetration depths into the bulk of the superlattice.

As a first example of a surface phase transition in a superlattice we consider a finite Fe/Cr- or Gd/Y-type structure. We assume that the temperature is low enough that all spins have a thermal averaged moment equal to their maximum value. Furthermore we assume that the exchange coupling between atomic layers is sufficiently strong that the spins within a film are rigidly coupled together. These assumptions are reasonable for Fe/Cr or Co/Ru superlattices at room temperature.

For in infinitely extended Fe/Cr-type structure in an external field one expects a canted configuration as discussed earlier. From energy considerations, it is easy to show that the uniform canting angle is given by the equation

$$\cos\alpha_0 = H_0 M/4J \tag{18}$$

where M is the net magnetic moment of a film and J is the interface exchange energy. In a finite multilayer, however, this uniformly canted state is not stable [60]. As mentioned above, the reason for this is that the outer layers of the finite structure experience only half the exchange coupling of the interior layers and thus are easier to turn toward the applied field.

Stable ground state configurations for finite Fe/Cr type multilayers have been found [60] using the numerical method outlined above. These states are compared to the uniform canting state in figure 15. The structure in figure 15(b), the low-field case, is quite complex. The outermost spins are twisted into the direction of the field as expected, but the spins of the second layer are actually turned farther away from the field than they would be in the bulk configuration. This alternation continues as one progresses into the bulk of the superlattice, but the amplitude of the deviation decreases with increasing distance from the surface. The main difference between the configurations of figure 15(b) and that found in figure 15(c) is that there is no alternation in the high-field configuration of figure 15(c).

The surface twist states illustrated in figure 15(b) and (c) reduce the energy of the structure as compared to the uniform canting state by lowering the Zeeman energy. (As a result the surface twisted states have a slightly higher magnetization than does the uniformly canted state.) However the twist also results in a small increase of exchange energy. The resulting structure is as usual a compromise between exchange and Zeeman energy. It is worthwhile to compare these non-uniform canted structure discussed here to the very different case of non-uniform canting found in a domain wall. For example, the width of a domain wall in a ferromagnet is governed by the competition between the exchange energy and the anisotropy energy. The exchange energy can be minimized by spreading the canting out over many layers of spins and thus favours a very extended wall. In contrast, the anisotropy energy is minimized when spins point in the easy direction, thus favouring a narrow wall. In the surface-twist problem the competition is between exchange and Zeeman energies, and there is also the additional freedom of having *two sublattices*. This allows new kinds of state to occur when minimizing the total energy. The alternating spin configuration seen in figure 15(b), for example, has the exchange energy between layers of spins alternately increase and decrease as one moves through the multilayer. This extra

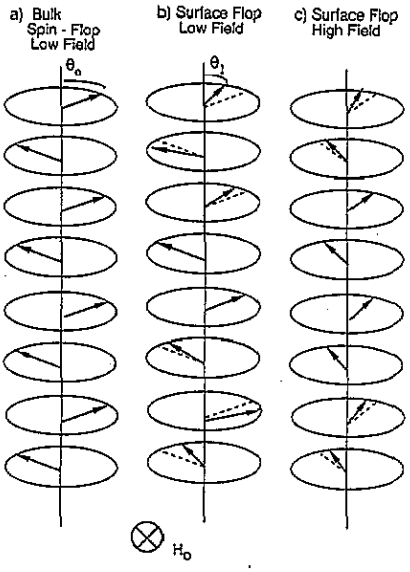

Figure 15. Examples of possible configurations for a multilayer composed of antiferromagnetically coupled ferromagnetic thin films. The magnetization of each thin film n lies in the plane of the film and is represented by an arrow; it makes an angle θ_n with the external field H_0. (*a*) The 'bulk' state, where θ_n is the same for all films. (*b*) and (*c*) Configurations for a finite multilayer, with the upper part of the diagram being the top surface of the multilayer and the lower part the bottom surface of the multilayer. The broken lines in (*b*) and (*c*) show the 'bulk' configuration for these cases. Note that for (*b*) the outermost spins are turned into the direction of the field, but that the next layer has the spins turned away from the field when compared to the bulk configuration. (After [60].)

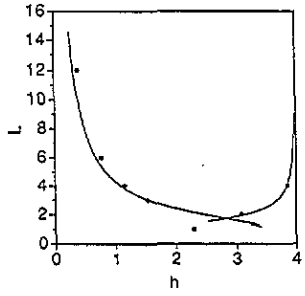

Figure 16. Results of the variational calculation for the penetration length L as a function of applied field. The full curves represent the results of the variational calculations and the filled circles are the equivalent results from the numerical calculation. Note the rapid increase in L at both high and low fields. (After [60].)

degree of extra freedom allows the width of the non-uniform canting region to vary in an interesting manner as a function of applied field. At low fields the non-uniform region is very large; for moderate fields it is quite small and then for larger fields the width of the non-uniform regions is again large.

A variational calculation [60] gives a simple result for the width of the non-uniform canting region. We define a dimensionless measure of the applied field as

$$h = H_0 M/|J|. \tag{19}$$

The length of the non-uniform surface twist is then given approximately by the expression

$$L = 1 + \sqrt{\frac{12}{h^2}} - 1 \tag{20}$$

where L is the number of films involved in the surface twist. This result is only valid for small h. A comparison of the variational results for L with the results carried out within the iterative model discussed above is presented in figure 16.

A second system which displays a surface phase transition is a finite Fe/Gd superlattice. In this case the surface phase transition depends on the nature of the outermost film [59]. We consider an Fe/Gd system constructed so that at low temperatures and fields the system is in a Gd-aligned phase. If the outermost film is Fe then increasing the field causes a phase transition from the Gd-aligned state to a surface-twisted state. This transition nucleates at the surface and occurs at a field which is about five times lower than that required for the bulk transition. In contrast, if the outermost film is Gd the phase transition from the aligned phase to the twisted phase begins in the interior of the sample.

It is easy to understand why the structure with Fe on the outside should have a surface phase transition. In the Gd-aligned phase the Gd spins point along the external field and the Fe spins are antiparallel to the external field. Fe spins in the interior are strongly held antiparallel to the external field by the antiferromagnetic coupling to the Gd spins on both sides of the Fe film. In contrast, Fe spins at the surface are not as strongly fixed since there are Gd spins on only one side of the Fe film. As a result, as the external field increases from zero, those Fe spins in the outermost layer are the first to turn toward the direction of the applied field. Thus the phase transition nucleates at the surface and occurs at fairly low values of field. On the other hand, if the outermost film is composed of Gd, the situation is very different. With Gd on the outside, then the spins in the outermost film are parallel with the external applied field in the Gd-aligned phase. Any increase in the external field tends to stabilize these outer spins in the direction of the field. Therefore, the phase transition in this case is essentially a bulk phenomenon, and, in fact, for thin films the phase transition can actually be somewhat suppressed.

An analogous phenomenon occurs in the transition from the Fe-aligned phase to the canted phase. In the Fe-aligned phase, the Gd spins are antiparallel to the external field. As a result if the outer layer is composed of Gd, then the phase transition nucleates at the surface. On the other hand, if Fe is on the outside, then the phase transition nucleates in the interior of the crystal. This phase transition is thus essentially a bulk phenomenon and so occurs near the bulk value.

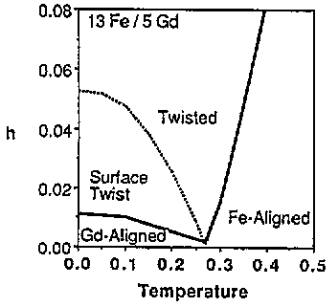

Figure 17. Phase diagram for bulk and surface phase transitions in a $[13\ Fe/5\ Gd]_{10}/13$ Fe superlattice. h and t are unitless measures of the external magnetic field and temperature as described in figure 6. The dotted curve represents the transition to the twisted phase in an infinite Fe/Gd superlattice. (After [59].)

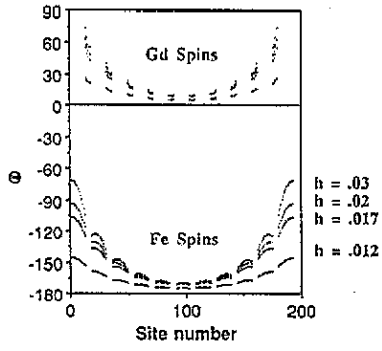

Figure 18. The angle that the spins in an Fe/Gd superlattice make with respect to the applied field as a function of position for a ten-unit cell 13 Fe/5 Gd superlattice. As the external field h is increased the reconstructed state deviates significantly from the aligned state. (After [59].)

The phase diagram for the finite Fe/Gd superlattice can be readily obtained by use of the iterative energy minimization method described above. The results are presented in

figure 17. Here we consider a [13 layer Fe/5 layer Gd]$_{10}$/13 layer Fe superlattice. We see that the aligned-Gd state now occupies only a small region of the phase diagram and that the surface-twist state occurs at much lower fields than is found in the bulk system. The structure of the reconstructed state is presented in figure 18. We see that even for fields well below that necessary to cause the bulk transition to the twisted state ($h = 0.052$) there are large deviations from the aligned state structure. The penetration depth of surface deviation is of the order of 3–4 unit cells which can be a length of a few hundred Ångströms.

In this section we have shown that a position-dependent energy minimization scheme which takes into account both the thermal averaged magnitude of the magnetic moments and their orientation can give a good account of the magnetic structure for many different magnetic multilayer systems. The general behaviour of magnetic multilayers as a functions of both temperature and applied field can be straightforwardly predicted. This provides an understanding of both macroscopic measurements such as $M(T)$ and static susceptibility as well as microscopic measurements such as neutron scattering and Mössbauer studies.

The method developed here and variations of this method [61] have also been used to study a number of other multilayer systems. These include magnetic structures in quasi-periodic superlattices [62], antiferromagnetic superlattices [38], ferromagnetic/antiferromagnetic multilayers [63] and thin Gd films on Fe substrates [32]. The magnetic structure as a function of applied field can also be used to calculate magnetoresistance [55]. Finally, we note that a correct ground state is necessary for calculations of dynamic properties such as spin wave modes. This will be explored further in the next section.

3. Spin-wave excitations in magnetic multilayers

3.1. Introduction

As we have seen, much of the most interesting physics that occurs in magnetic multilayers is due to the coupling across interfaces and the effects of having a surface. Unfortunately the nature and strength of interactions across an interface are difficult to measure directly. Even with techniques such as SPLEED and neutron scattering [64, 65], it is difficult to obtain unambiguous information on the magnetic structure of surfaces and interfaces. Measurements of the static magnetization of magnetic multilayers are usually limited to detecting the averaged magnetic moment from a relatively large volume of sample. Another problem, for example, is that ferromagnetic interlayer exchange coupling cannot always be inferred from static magnetization measurements.

One method of investigating surface and interface magnetism, which has proven useful in studies of ferromagnetic films and multilayers, is to probe the spin-wave excitations of a magnetic system [66, 67]. In a spin wave the magnetic moments at each site precess about their individual equilibrium directions. Since the spins are coupled with one another through exchange and dipolar interactions, spin-wave excitations are the eigenmodes of the magnetic system and are characterized by frequency and wavelength. Thus the frequency of a spin wave may depend quite sensitively on the exchange coupling between spins as well as other effective fields caused by, for example, anisotropies and magnetoelastic effects. These interactions will not only affect the frequency of precession but also the relative phase of precession between spins at neighbouring lattice sites.

In ferromagnetic systems such as Fe and Co the lowest spin-wave frequencies are typically of the order of 10 GHz. These are long-wavelength excitations and can be studied using ferromagnetic resonance and Brillouin light scattering techniques [68–71]. Higher energy excitations can be observed by magnetic neutron scattering [72, 73]. Spin-wave

frequencies in antiferromagnetic compounds are typically much higher, existing at several hundred GHz, and thus also influence the optical properties in the infrared region [74–76]. Excitations in antiferromagnets can be observed with Raman scattering as well as neutron scattering [67, 73]. In magnetic multilayers, the energies of long-wavelength spin-wave excitations will also range from a few GHz to several hundred GHz depending on the choice of constituent materials. We note however, that one of the fascinating aspects of spin waves in magnetic multilayers is that their energies can be made to vary over a fairly large range simply by changing the relative thicknesses of the constituent materials. Finally, the presence of surfaces and interfaces can lead to a localization of spin-wave modes to the boundaries between materials and to the outer layers of a finite multilayer [77]. These localized modes thus make ideal probes for examining surface and interface conditions [78].

Finally, spin-wave excitations are also important for thermodynamic properties [79, 80]. Spin waves are bosons whose number depends on the temperature of the system. The presence of spin-wave excitations thus reduce the net magnetic moment along the direction of magnetization. In a superlattice structure, gaps in the spin-wave spectrum appear due to the periodicity of the system. Clearly these can play an important role in the thermodynamic behaviour. There are several works using linear spin-wave theory to estimate $M(T)$ at low temperatures in multilayer and superlattice structures [81–84]. Non-linear spin-wave interactions are also interesting and become important in determining $M(T)$ at higher temperatures [85, 86]. Non-linear interactions also lead to unique high-power resonance behaviour and non-linear optical properties [87, 88].

3.1.1. General features of excitations in multilayers. Before discussing the details of spin waves in magnetic multilayers, we first review in very general terms some of the fundamental concepts of superlattice and multilayer excitations. We begin by examining the modes of a system of coupled oscillators. First imagine a system of $2N$ uncoupled pendula. We assume that the pendula are identical so that the frequency of small oscillations for each pendulum is ω_0. In this system, the oscillations of each pendulum are completely independent of each other and so there are no correlations between the motions of any of the pendula. If we were to drive the motion of the system by applying some oscillating external force, the only strong response we would observe would occur when the driving frequency was equal to ω_0.

Suppose now that we couple each pendulum to one of its nearest neighbours using springs as shown in figure 19(a). The strength of each spring in characterized by a constant C_1. We can now think of our system of $2N$ pendula as a system of N sets of two coupled pendula. The motions of the individual pendula within each coupled pair are now strongly correlated. This results in two normal modes for each pair with each motion corresponding to a different frequency of oscillation. These motions are sketched in figure 19(b) and (c). The motion in (b) is characterized by the two pendula oscillating in phase with one another and the motion in (c) is characterized by the two pendula oscillating exactly 180° out of phase with one another. The frequency of the motion in (b) will be ω_0, whereas the frequency of the motion in (c) will be $\omega_0 + \Delta$ which is larger than ω_0, due to the added energy involved in stretching and compressing the coupling spring. Since the relative motions between pendula pairs are still completely uncorrelated, the system of $2N$ pendula would show a response to a driving force at only two frequencies: ω_0 and $\omega_0 + \Delta$.

If we add springs of spring constants C_1 between all neighbouring pendula we than have a system of $2N$ coupled oscillators. This results in $2N$ different possible modes, each being characterized by a frequency and also by a relative phase angle between the oscillations of neighbouring pendula. The system will show a response to a driving force at $2N$ possible

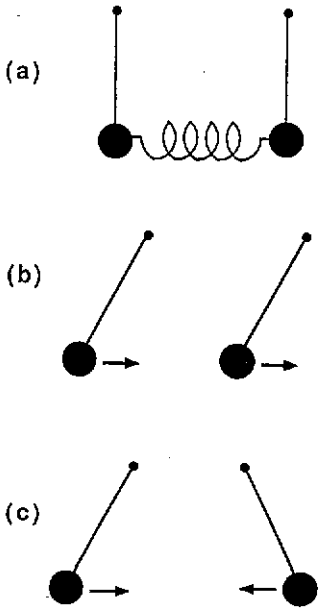

Figure 19. (*a*) Two pendula coupled by a spring. The two possible motions are (*b*) an in-phase oscillation and (*c*) an out-of-phase oscillation.

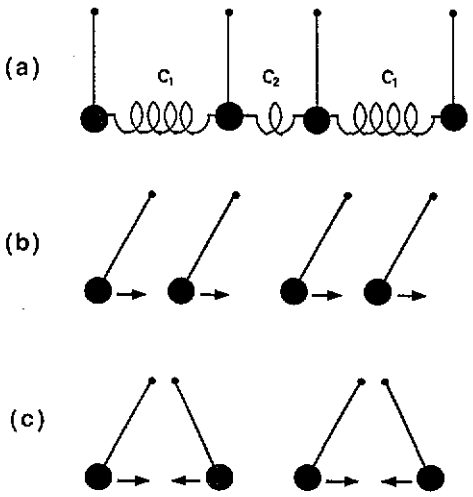

Figure 20. (*a*) A 'superlattice' of pendula where every pendulum is coupled to its nearest neighbours via springs. The spring constants alternate between C_1 and C_2. Viewed as *pairs* of pendula coupled by C_2 springs, the lowest-frequency motions are in-phase oscillations of the pendula pairs. Since there are two types of internal motion of the pendula pairs, the longest-wavelength motions of the entire system appears as in (*b*) and (*c*).

frequencies. The relative phase angle between oscillations defines a wavelength. The mode where all of the pendula oscillate in phase with one another has frequency ω_0 and a corresponding wavelength of infinity.

A superlattice or multilayer is constructed in a slightly different way. Consider again the system of N coupled pendula pairs. Recall that each pair of pendula is internally coupled by a spring with spring constant C_1. Let us now couple each pair with both of its neighbours by a different spring constant C_2 which we will assume is much smaller than C_1. This construction is shown schematically in figure 20(*a*). There will now be two general classes of excitation corresponding to the two modes of oscillation of each pendula pair. The low-frequency excitations are composed of the in-phase pendula pair oscillations. A long-wavelength example is sketched in figure 20(*b*). The different modes corresponding to different phase angles between the oscillations of neighbouring pendula *pairs* form a band of excitations. Similarly there is a band of N modes due to the out-of-phase pendula pair oscillations. A long-wavelength excitation for this band is sketched in figure 20(*c*). The frequencies of these modes are in general higher than those of the other band by approximately Δ.

The superlattice described above is constructed out of sets of coupled pendula. The number of bands depends on the number of 'internal' motions of each set of coupled pendula. Thus, if we had built the superlattice out of $N/2$ sets of four coupled pendula, we would have four bands of modes. There would be $N/2$ modes in each band.

A well known example of excitations in a periodic system is the allowed energy states of the one-dimensional Kronig–Penney model [89]. This model consists of finite potential wells arranged periodically in a row. Standing-wave solutions of an electron wave function exist inside each well, and exponentially decaying waves are allowed in the regions between wells. The resulting collective excitations are Bloch wave states and are the excitations in the individual wells modulated by a function that has the periodicity of the lattice. In terms of our pendula analogy, the modes of a coupled pendula pair correspond to the standing-wave solutions in the potential wells. The springs C_2 provide a coupling mechanism corresponding to the exponentially decaying waves between wells. The Bloch wavevector is proportional to the inverse of a wavelength that specifies the relative phase between the standing-wave functions in neighbouring potential wells.

3.1.2. Spin-wave excitation in thin films. In order to discuss spin-wave excitations in magnetic multilayers in the light of the coupled-pendula analogy presented above, we must first identify the 'pendulum' components for a magnetic multilayer. These are simply the allowed spin-wave excitations of a magnetic film. The coupling 'springs' between the spin-wave excitations of the individual films can be due to both dipolar fields and exchange coupling between the films. The first part of this section is concerned with how the spin-wave excitations of each film of a magnetic multilayer couple together through purely dipolar interactions. The effects of exchange coupling will be considered later.

We now discuss long-wavelength low-energy excitations that can be detected using ferromagnetic resonance and Brillouin light scattering techniques. For sufficiently long wavelengths, the dynamic magnetic properties of the material can be described by a position-independent magnetic susceptibility χ of the form

$$\boldsymbol{m} = \chi \cdot \boldsymbol{h} \tag{21}$$

where $\boldsymbol{m}$ is a time and spatially varying component of the magnetization and $\boldsymbol{h}$ is a time and spatially varying component of the magnetic dipolar field. Furthermore, we assume that the wavelengths of the excitations are still *short* enough that

$$(2\pi/\lambda)c \gg \omega. \tag{22}$$

In this limit, the magnetic fields in Maxwell's equations are uncoupled from electric fields. This is called the magnetostatic limit. The wavelengths λ for which both the approximations of equations (21) and (22) hold are typically from 10^{-3} to 10^{-7} m for ferromagnets.

The description of spin waves in this limit proceeds as follows. First an expression for χ is found by solving the Landau–Liftschitz equations of motion. These equations have the form

$$(\mathrm{d}/\mathrm{d}t)\boldsymbol{m} = \gamma \boldsymbol{m} \times (\boldsymbol{h} + \boldsymbol{H}_{\mathrm{eff}}) \tag{23}$$

where $\boldsymbol{H}_{\mathrm{eff}}$ is an effective field containing external applied fields, effective anisotropy fields and exchange fields. γ is the gyromagnetic ratio. For a ferromagnet without anisotropies, χ can be shown to have the well known form [90]

$$\chi = \frac{M_s}{H_0^2 - (\omega/\gamma)^2} \begin{bmatrix} H_0 & \mathrm{i}\omega/\gamma \\ -\mathrm{i}\omega/\gamma & H_0 \end{bmatrix} \tag{24}$$

where H_0 is an external applied field and M_s is the saturation magnetization. Note that exchange fields do not appear for a simple ferromagnet. This is only true for long-wavelength excitations where locally the spins are parallel. Thus the exchange field produces

no contribution to the torques experienced by a spin. This is not true for spin configurations where the spin orientations vary from layer to layer as in many of the structures discussed in section 2.

The constitutive relation between $\boldsymbol{m}$ and $\boldsymbol{h}$ given by equation (21) allows us to write the magnetostatic form of Maxwell's equations solely in terms of $\boldsymbol{h}$:

$$\boldsymbol{\Delta} \times \boldsymbol{h} = 0 \tag{25}$$

$$\boldsymbol{\Delta} \cdot \boldsymbol{b} = \boldsymbol{\Delta} \cdot (\mathbf{1} + 4\pi\chi)\boldsymbol{h} = \mathbf{0}. \tag{26}$$

Equation (25) allows us to define a magnetic potential ϕ such that

$$\boldsymbol{h} = -\boldsymbol{\Delta}\phi. \tag{27}$$

Using this in equation (26) gives [91]

$$\left[\partial^2/\partial z^2 + (1 + 4\pi\chi_{xx})(\partial^2/\partial y^2 + \partial^2/\partial x^2)\right]\phi = 0. \tag{28}$$

The solutions to this equation represent travelling waves and are assumed to have the form

$$\phi = \phi_0 \exp\left[\mathrm{i}(\boldsymbol{q}_\parallel \cdot \boldsymbol{x}_\parallel - \omega t)\right]. \tag{29}$$

The vectors $\boldsymbol{q}_\parallel$ and $\boldsymbol{x}_\parallel$ are the wave and position vectors parallel to the surfaces. In a film geometry, the solutions also have to obey the boundary conditions at the surfaces which follow from Maxwell's equations. These require that the normal components of $\boldsymbol{b} = (1 + 4\pi\chi)\boldsymbol{h}$ and the tangential components of $\boldsymbol{h}$ be continuous across the surfaces.

The solution of equation (28) has the form

$$\phi = \left[A \exp(\mathrm{i}ky) + B \exp(-\mathrm{i}ky)\right] \exp(\mathrm{i}\boldsymbol{q}_\parallel \cdot \boldsymbol{x}_\parallel) \tag{30}$$

where the surface normal is taken to be in the y direction. Only discrete values of k will be allowed by the boundary conditions. For real k, these solutions describe guided waves which propagate in the film. These kinds of wave are called bulk or volume modes.

A second type of solution occurs when k is imaginary. The wave will then have its greatest amplitude near the surfaces of the film and its smallest amplitude in the bulk of the film. These kinds of waves are called surface modes. The amplitude of the field from a surface mode is relatively large outside the film in comparison to that from a bulk mode which is localized inside the film. One can show that the fields of a surface mode extend a characteristic distance $1/|\boldsymbol{q}_\parallel|$ outside the film.

Application of the boundary conditions results in an implicit dispersion relation relating $\boldsymbol{q}_\parallel$ and ω:

$$q_\parallel^2 + 2q_\parallel k(1 + 4\pi\chi_{xx}) \cot(kL) - k^2(1 + 4\pi\chi_{xx})^2 - 16\pi^2 q_z^2 \chi_{xy}^2 = 0 \tag{31}$$

with

$$k = \mathrm{i}\left[q_x^2 + q_z^2/(1 + 4\pi\chi_{xx})\right]^{1/2}. \tag{32}$$

Solutions of this relation are shown in figure 21. The frequencies are shown as functions of the wavevector $|\boldsymbol{q}_\parallel$ where $\boldsymbol{q}_\parallel$ is in the plane of the film. The lower set of modes are

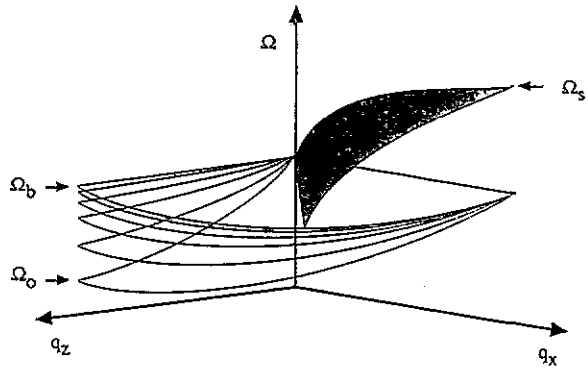

Figure 21. Dipolar magnetostatic spin waves for a ferromagnetic film. The frequencies are shown as functions of both q_y and q_z where q is the in-plane component of the wavevector. The applied field is in the z direction. The bulk modes exist in the frequency region between $\Omega_0 = \gamma H_0$ and $\Omega_B = \gamma[H_0(H_0 + 4\pi M_s)]^{1/2}$. A surface mode exists between Ω_B and $\Omega_S = \gamma(H_0 + 2\pi M_s)$ for some directions of propagation. (After [92].)

all bulk modes and the highest-frequency mode is a surface mode. The surface mode has the interesting property that it propagates only for a restricted set of directions with respect to the applied field. For propagation along the x direction, the surface mode is localized to top side of the film, while for propagation along the $-x$ direction, the surface mode is localized to the bottom side of the film.

For propagation perpendicular to the applied field direction on a semi-infinite ferromagnetic, the results take simple forms. The surface wave (often referred to as the Damon–Eshbach mode [92]) has frequency

$$\omega_s = \tfrac{1}{2}\gamma\left(H_0 + B\right) \tag{33}$$

where B is $H_0 + 4\pi M_s$. The bulk modes are degenerate for this propagation direction with frequency

$$\omega_b = \gamma\sqrt{H_0 B}. \tag{34}$$

3.2. Spin waves in superlattices

Consider a superlattice constructed by alternating magnetic films with non-magnetic films. The spin-wave modes of each magnetic film can then couple across the non-magnetic layers to form collective spin-wave excitations of the superlattice. The strength of the coupling depends on the amplitude of the fields in the non-magnetic layers. However, as we have seen from the previous section, of all the allowed modes of a film the surface mode has the largest field amplitudes outside the film. Thus the strongest coupling due to dipolar interactions occurs between the surface waves of individual magnetic films.

The magnetic potential ϕ of a possible superlattice mode is sketched in figure 22 as a function of position in the superlattice. It is composed of surface waves on the individual films, but its amplitude is modulated by a periodic 'envelope' function. Since the envelope function is periodic, the superlattice mode shown here is a collective 'bulk' wave even though it is composed of surface waves on the individual films. Later we will also see that collective modes can exist on semi-infinite superlattices and finite multilayers and are localized to the outermost layers of a structure as 'surface' modes.

3.2.1. Transfer matrix description. A simple but powerful technique can be used to describe superlattice excitations. This technique is known as the transfer matrix method [93, 94]. The method is basically as follows. The amplitudes of the fields at an interface between two

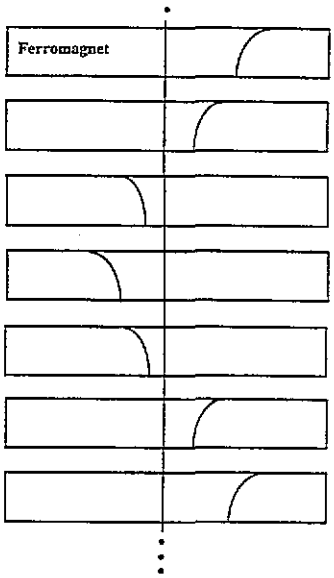

Figure 22. Amplitude of the scalar magnetic potential as a function of position in a magnetic superlattice for a bulk mode. The excitations in each magnetic film are surface modes and localized to one surface of the film. The collective excitation is oscillatory and is therefore a bulk mode of the superlattice. (After [95].)

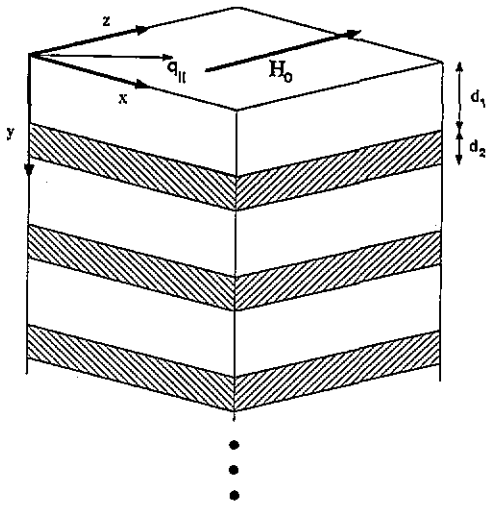

Figure 23. Multilayer and superlattice geometry. The applied field is in the z direction and an in-plane wavevector q is defined in the xz plane. The thickness of each magnetic film is d_1 and the thickness of each non-magnetic film is d_2.

films are written in terms of the amplitudes of the fields at the neighbouring interface. This process is continued until the amplitudes of the fields at one side of a unit cell of the superlattice are related to the amplitudes of the fields at the other side of the unit cell. This relationship is conveniently written in matrix form and is called the transfer matrix. For an infinitely extended superlattice, Bloch's theorem can be applied and the eigenvalues of the allowed superlattice excitations found. Alternatively, repeated application of this matrix can be used to relate the fields at one end of a finite multilayer to the fields at the other end of a multilayer, and find the allowed eigenvalues.

First we describe the geometry of the superlattice shown in figure 23. The thickness of each magnetic film is d_1 and the thickness of each non-magnetic film is d_2. The axis of the superlattice is set in the y direction and the films are indexed by the integer n. The length of a unit cell is defined as

$$L = d_1 + d_2.$$

We begin the calculation by defining the form of the waves which can exist in the superlattice. The waves which can exist in the magnetic film are defined similarly to equation (30):

$$\Phi_n^{\text{magnetic}} = \Big\{ A_n \exp[\alpha(y - nL - d_1)] + B_n \exp[-\alpha(y - nL)] \Big\} \exp\big[\mathrm{i}(q_{\|} \cdot x_{\|} - \omega t)\big] \qquad (35)$$

for $nL < y < nL + d_1$. The decay constant α is assumed to be real and is determined by solving equation (28). The solution is simply $\alpha = \mathrm{i}k$ where k is given in equation (32).

The waves in the non-magnetic films are defined similarly:

$$\Phi_n^{\text{non-magnetic}} = \left\{C_n \exp\left\{q_\parallel[y-(n+1)L]\right\} + D_n \exp\left[-q_\parallel(y-nL-d_1)\right]\right\} \exp\left[i(q_\parallel \cdot x_\parallel - \omega t)\right] \tag{36}$$

for $nL + d_1 < y < (n+1)L$. Here the decay constant has already been determined by Maxwell's equations and is equal to the magnitude of the parallel wavevector.

We now apply the electromagnetic boundary conditions at $y = nL+d_1$ and $y = (n+1)L$. Continuity of the tangential h components leads to

$$A_n + B_n \exp(-\alpha d_1) = C_n \exp(-q_\parallel d_2) + D_n \tag{37}$$

and

$$A_{n+1} \exp(-\alpha d_1) + B_{n+1} = C_n + D_n \exp(-q_\parallel d_2). \tag{38}$$

Continuity of the normal components of b results in

$$A_n \lambda_+ + B_n \lambda_- \exp(-\alpha d_1) = q_\parallel \left(C_n \exp(-q_\parallel d_2) - D_n\right) \tag{39}$$

and

$$A_{n+1}\lambda_+ \exp(-\alpha d_1) + B_{n+1}\lambda_- = q_\parallel \left[C_n - D_n \exp(-q_\parallel d_2)\right]. \tag{40}$$

In the last two equations, we have used

$$\lambda_\pm = iq_x \chi_{yx} \pm \alpha(1 + \chi_{yy}). \tag{41}$$

Our goal is to have two equations relating A_n, B_n and A_{n+1}, B_{n+1}. We do this by eliminating C_n and D_n from the above four equations. Using the definitions

$$\Gamma_{\pm\pm} = \lambda_\pm + q_\parallel \tag{42}$$

and

$$\mathbf{T} = \frac{1}{\Gamma_{++}\Gamma_{--} - \Gamma_{+-}\Gamma_{-+}} \times \begin{bmatrix} e^{\alpha d_1}[E_+\Gamma_{++}\Gamma_{--} - E_-\Gamma_{+-}\Gamma_{-+}] & 2\cosh(q_\parallel d_2)\Gamma_{--}\Gamma_{-+} \\ -2\cosh(q_\parallel d_2)\Gamma_{++}\Gamma_{+-} & e^{-\alpha d_2}[E_-\Gamma_{++}\Gamma_{--} - E_+\Gamma_{+-}\Gamma_{-+}] \end{bmatrix} \tag{43}$$

where $E_+ = \exp(q_\parallel d_2)$ and $E_- = \exp(-q_\parallel d_2)$, the result can be put in the compact form

$$\begin{pmatrix} A_{n+1} \\ B_{n+1} \end{pmatrix} = \mathbf{T} \begin{pmatrix} A_n \\ B_n \end{pmatrix}. \tag{44}$$

The matrix $\mathbf{T}$ in equation (43) is called the transfer matrix. This matrix has the property that its determinant is equal to unity, which is a statement of energy conservation within the superlattice. In the following sections we will use this matrix to examine the bulk and surface spin-wave modes of a magnetic superlattice.

3.2.2. Bulk spin waves in superlattices. We first illustrate the use of the transfer matrix method by finding the dispersion relation of bulk spin waves in a superlattice. This is done by requiring the amplitudes A_n and B_n to have the periodicity of the superlattice structure. This is a statement of Bloch's theorem for a periodic structure:

$$\begin{pmatrix} A_{n+1} \\ B_{n+1} \end{pmatrix} = \exp(\mathrm{i}QL) \begin{pmatrix} A_n \\ B_n \end{pmatrix} \tag{45}$$

where Q is the Bloch wavevector for the collective excitation.

Using equation (44) together with equation (45), we can write

$$\left[\mathbf{T} - \exp(\mathrm{i}QL)\mathbf{I}\right] \begin{pmatrix} A_n \\ B_n \end{pmatrix} = 0 \tag{46}$$

and equivalently,

$$\left[\mathbf{T}^{-1} - \exp(-\mathrm{i}QL)\mathbf{I}\right] \begin{pmatrix} A_n \\ B_n \end{pmatrix} = 0 \tag{47}$$

where $\mathbf{T}^{-1}$ is the inverse of $\mathbf{T}$. These two equations can be combined to give

$$\cos(QL) = \tfrac{1}{2}\left(\mathbf{T} + \mathbf{T}^{-1}\right) = \tfrac{1}{2}\mathrm{tr}\,\mathbf{T} \tag{48}$$

where tr stands for the trace. This expression gives an implicit dispersion relation for bulk spin waves in the superlattice structure.

Equation (48) can be written in the form

$$\cos(QL) = \left\{\left[q_\parallel^2 + \alpha^2\left(1 + \chi_{yy}\right)^2 + q_x^2\chi_{yx}^2\right]/2q_\parallel\alpha\left(1 + \chi_{yy}\right)\right\}\sinh(\alpha d_1)\sinh(q_\parallel d_2) + \cosh(\alpha d_1)\cosh(q_\parallel d_2). \tag{49}$$

This dispersion has the same form as that obtained in the standard electronic Kronig–Penney model. As in the electronic problem, gaps appear in the spin-wave spectrum due to the periodicity of the structure. Explicit results for surface and bulk spin waves in superlattices are discussed in the next section.

3.2.3. Surface spin waves in superlattices. As we saw in section 3.1.2, the presence of surfaces can lead to surface-localized excitations in thin magnetic films. This is also true in superlattice structures. To see this, we now search for surface excitations on a semi-infinite magnetic superlattice. As in figure 23, we locate the outermost surface of the superlattice at $y = 0$. This corresponds to placing the surface at the first interface of the $n = 0$ unit cell. The superlattice extends through the $y > 0$ half space, and we assume that the $y < 0$ half space is vacuum.

The presence of a surface at $y = 0$ means that we must now define a magnetic potential for the $y < 0$ region. We choose a form that represents exponential decay in the $-y$ direction:

$$\Phi^{\text{outside}} = \Phi_0 \exp(q_\parallel y)\exp\left[\mathrm{i}\left(q_\parallel \cdot x_\parallel - \omega t\right)\right]. \tag{50}$$

The decay constant $q_\parallel$ was determined by the Maxwell equation $\boldsymbol{\Delta} \cdot \boldsymbol{b} = 0$.

The requirement that the scalar potential satisfy the electromagnetic boundary conditions at $y = 0$ leads to two equations involving A_0 and B_0. Continuity of tangential h leads to

$$\Phi_0 = A_0 \exp(-\alpha a) + B_0 \tag{51}$$

and continuity of normal b results in

$$q_\parallel \Phi_0 = A_0 \exp(-\alpha s)\lambda_+ + B_0 \lambda_-. \tag{52}$$

Using the relations given in equations (51) and (52), we eliminate Φ_0 from these two equations to find

$$B_0/A_0 = -\exp(-\alpha s)\Gamma_{+-}/\Gamma_{--}. \tag{53}$$

In the superlattice region $y > 0$, we also require that the collective excitation decay exponentially away from the surface with increasing y. We thus write

$$\begin{pmatrix} A_{n+1} \\ B_{n+1} \end{pmatrix} = \exp(-\beta L) \begin{pmatrix} A_n \\ B_n \end{pmatrix} \tag{54}$$

where β is positive and real.

Using this requirement in equation (44), we obtain for the case $n = 0$ the expression

$$\mathbf{T} \begin{pmatrix} A_0 \\ B_0 \end{pmatrix} = \exp(-\beta L) \begin{pmatrix} A_0 \\ B_0 \end{pmatrix}. \tag{55}$$

Defining the components of $\mathbf{T}$ as T_{ij}, this matrix equation consists of two coupled equations:

$$T_{11} A_0 + T_{12} B_0 = \exp(-\beta L) A_0 \tag{56}$$

and

$$T_{21} A_0 + T_{22} B_0 = \exp(-\beta L) B_0. \tag{57}$$

Eliminating $\exp(-\beta L)$ between these two equations, we obtain an implicit dispersion relation for the superlattice surface mode:

$$T_{11} - T_{22} + T_{12}(B_0/A_0) - T_{21}(A_0/B_0) = 0. \tag{58}$$

Using equations (43) and (53), this can be written simply as

$$\sinh(\alpha a)\Gamma_{+-}\Gamma_{--} = 0. \tag{59}$$

Equation (59) has three possible solutions. These are $\Gamma_{+-} = 0$, $\Gamma_{--} = 0$, and $\sinh(\alpha a) = 0$. We can determine which of these represents a true surface mode by solving for β. We examine below each of these possible solutions in turn.

(1) $\Gamma_{+-} = 0$ requires $\beta = -(\alpha d_1 + q_\parallel d_2)$. This would imply that the collective excitation exponentially increases in the superlattice away from the surface rather than decreasing. This possibility does not represent a true surface mode.

(2) $\Gamma_{--} = 0$ requires $\beta = \alpha d_1 - q_\parallel d_2$. As long as αd_1 is greater than $q_\parallel d_2$, this solution represents a true surface mode. This gives an interesting condition for the existence of a

surface mode that depends on the relative thicknesses of the magnetic and non-magnetic layer thicknesses. For the special case of propagation perpendicular to the applied field in the x direction, this condition is simply that the thicknesses of the magnetic layers be greater than that of the non-magnetic layers. Finally, we note that this collective surface mode of the superlattice is composed of the surface modes from the individual magnetic films since α is real.

(3) The possibility that $\sinh(\alpha d_1) = 0$ can also be shown to represent surface modes in the following way. First, $\sinh(\alpha d_1) = 0$ when

$$\alpha = \mathrm{i}m\pi/d_1 \tag{60}$$

where m is an integer greater than or equal to 0. In order to show that these cases correspond to surface excitations, we need to find β. This is done by repeating the arguments of section 3.2.2, using $\exp(-\beta L)$ in place of the Bloch wave $\exp(\mathrm{i}QL)$. The result is similar in form to equation (49):

$$\cosh(\beta L) = \left\{\left[q_\parallel^2 + \alpha^2(1+\chi_{yy})^2 + q_x^2\chi_{yx}^2\right]/2q_\parallel\alpha(1+\chi_{yy})\right\}\sinh(\alpha d_1)\sinh(q_\parallel d_2) + \cosh(\alpha d_1)\cosh(q_\parallel d_2). \tag{61}$$

With the condition given by equation (61) such that $\sinh(\alpha d_1) = 0$, this expression simplifies to

$$\cosh(\beta L) = (-1)^m \cosh(q_\parallel d_2). \tag{62}$$

When m is even, then this represents a surface-wave solution with

$$\beta L = q_\parallel d_2. \tag{63}$$

When m is odd, then

$$\beta L = q_\parallel d_2 + \mathrm{i}\pi(2m+1). \tag{64}$$

The m-odd case also represents a surface-wave solution, but with a 180° phase shift between the excitations of neighbouring magnetic films. Since α is imaginary for this case, these collective surface modes are composed of bulk waves in the individual magnetic films.

To illustrate the difference between the two types of surface mode, in figure 24 we sketch the amplitude of the magnetic potential as a function of position in the superlattice for each type. In (a), we show the superlattice surface mode corresponding to $\Gamma_{--} = 0$ and in (b) we show a superlattice surface mode corresponding to $\sinh(\alpha d_1) = 0$ for $m = 2$. Both have amplitudes which are localized to the surface of the superlattice structure, but each is constructed from a different set of coupled modes.

It is also possible to obtain simple expressions for the frequencies of these surface modes. The surface mode sketched in figure 24(a), which consists of the coupled surface modes of each individual magnetic film, has a frequency given by $\Gamma_{--} = 0$. For propagation in the x direction perpendicular to the applied field, the frequency is identical to the frequency of the Damon–Eshbach surface wave on a semi-infinite ferromagnetic (equation (33)). Furthermore, it can also be shown that the superlattice surface mode is non-reciprocal with respect to propagation direction and does not exist for propagation in the $-q_x$ direction. This is also a feature common to the Damon–Eshbach mode of a semi-infinite ferromagnet.

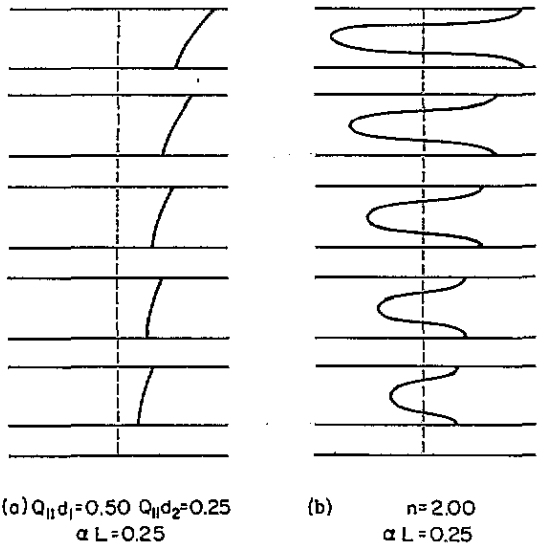

Figure 24. Amplitudes of the scalar magnetic potential for surface modes as a function of position in a semi-infinite magnetic superlattice. Two types of collective surface mode are possible: (*a*) ones composed of surface modes in the individual films, and (*b*) ones composed of bulk mode in the individual films. (After [9].)

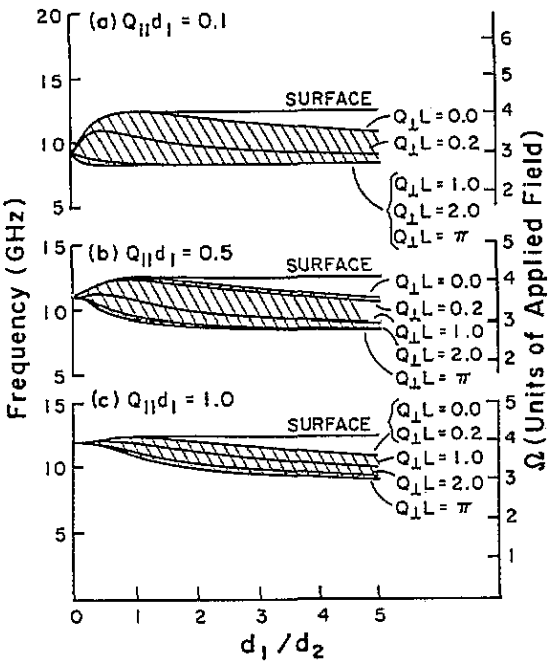

Figure 25. Frequencies of superlattice spin waves as functions of relative film thickness. The relative thicknesses of the magnetic and non-magnetic films is especially important for the surface modes—the surface mode exists only when the magnetic films are thicker than the non-magnetic films. Shown here are the spin-wave frequencies as functions of relative film thickness d_1/d_2 for three different choices of q. Propagation is perpendicular to the applied field. The shaded areas are the bulk modes, and $q_\perp$ is a measure of the perpendicular component of the wavevector. (After [9].)

The frequencies of the other surface modes are determined by equation (61). These frequencies are given by

$$\omega = \gamma\left\{H_0(H_0 + 4\pi M_s) - [4\pi M_s H_0/(1 + (m\pi/q_{\|}d_1)^2)](q_z/q_{\|})^2\right\}^{1/2}. \tag{65}$$

These modes are degenerate with the ferromagnetic resonance frequency for propagation perpendicular to the applied field.

An example of the bulk and surface mode frequencies as functions of relative layer thicknesses is shown in figure 25. Here propagation is perpendicular to the applied field.

The parameters used for this calculation are appropriate to an Ni/Mo superlattice with M_s = 480 G and an applied field strength of 1 kG. The shaded areas represent collective bulk modes and the full curves are the collective surface modes.

The band of bulk modes exists for frequencies between H_0B and $(H_0 + B)/2$. As $q_\parallel L$ increases, the frequency of a bulk mode decreases. For small $q_\parallel L$ the density of states is greatest near the bottom of the bulk bands. For larger $q_\parallel L$ the density of states becomes more uniform across the bulk band.

The surface-mode frequency is independent of the thickness ratio d_1/d_2 for $d_1 > d_2$. Its frequency is then identical to the Damon–Eshbach frequency for a surface mode on a semi-infinite ferromagnetic. For $d_1 < d_2$, the surface mode merges with the top of the bulk band and is no longer a true exponentially decaying surface mode of the structure.

In terms of the results from Brillouin light scattering experiments for this geometry, there should be three main contributions to the light scattering spectrum. The surface mode should contribute strongly for $d_1 \geqslant d_2$, with a frequency above that of the bulk modes. Also, the surface mode will exist only for certain propagation directions and therefore appear in only the Stokes or antistokes side of the light scattering spectrum. The other two features should be due to bulk modes. These modes should provide a strong but broad contribution from frequencies near the bottom of the bulk bands where the density of states is greatest. There should also be a large contribution from modes near the top of the bulk band. The reason is that the strength of the light scattering signal is in large part determined by the overlap of the electromagnetic fields of the incident light with the fields produced by the spin wave. Since an incident light wave has a limited penetration depth in a metallic superlattice, the magnitude of the overlap is determined over the first few hundred Ångströms of the superlattice. The higher-frequency bulk modes are characterized by small values of $q_\parallel L$ which means that the magnetic fields produced by the spin wave vary slowly as one moves away from the surface into the superlattice. The net value of the overlap of the light-wave and spin-wave fields is thus much larger for spin waves with small values of $q_\parallel L$ than for spin waves with large values of $q_\parallel L$.

In figure 26, we reproduce experimental light scattering spectra taken from Fe/Pd multilayers. The different spectra are results for multilayers with various thickness ratios for the magnetic and non-magnetic films. Note that for $d_1 > d_2$ there is an extra peak on the Stokes side which is due to a surface mode excitation. For $d_1 < d_2$ there are only two peaks visible in the spectrum. Note that the feature at Ω_b is an artifact of the calculation and does not represent a physical feature.

3.2.4. Spin waves in finite multilayers. The characteristics of spin waves on finite multilayers differ in many respects from those in semi-infinite superlattices. Some of the more important differences are as follows. There will only be as many modes as magnetic layers. So with N layers, there will be $N - 1$ collective bulk waves and one collective surface wave for each mode of the individual magnetic films.

Since there are two outside surfaces of the multilayer, there will be surface mode propagation in the $+x$ and $-x$ directions. The mode propagating to the left of the applied field will be localized to one surface of the multilayer and the mode propagating to the right of the field will be localized to the other surface of the multilayer. Furthermore, the surface-mode frequency will in general decrease with decreasing number of layers in the multilayer.

The rule that a surface mode exists only when the thickness of the magnetic film is greater than that of the non-magnetic film also does not hold for multilayers with small numbers of layers [96]. For numbers of layers of the order of ten, the non-magnetic layer

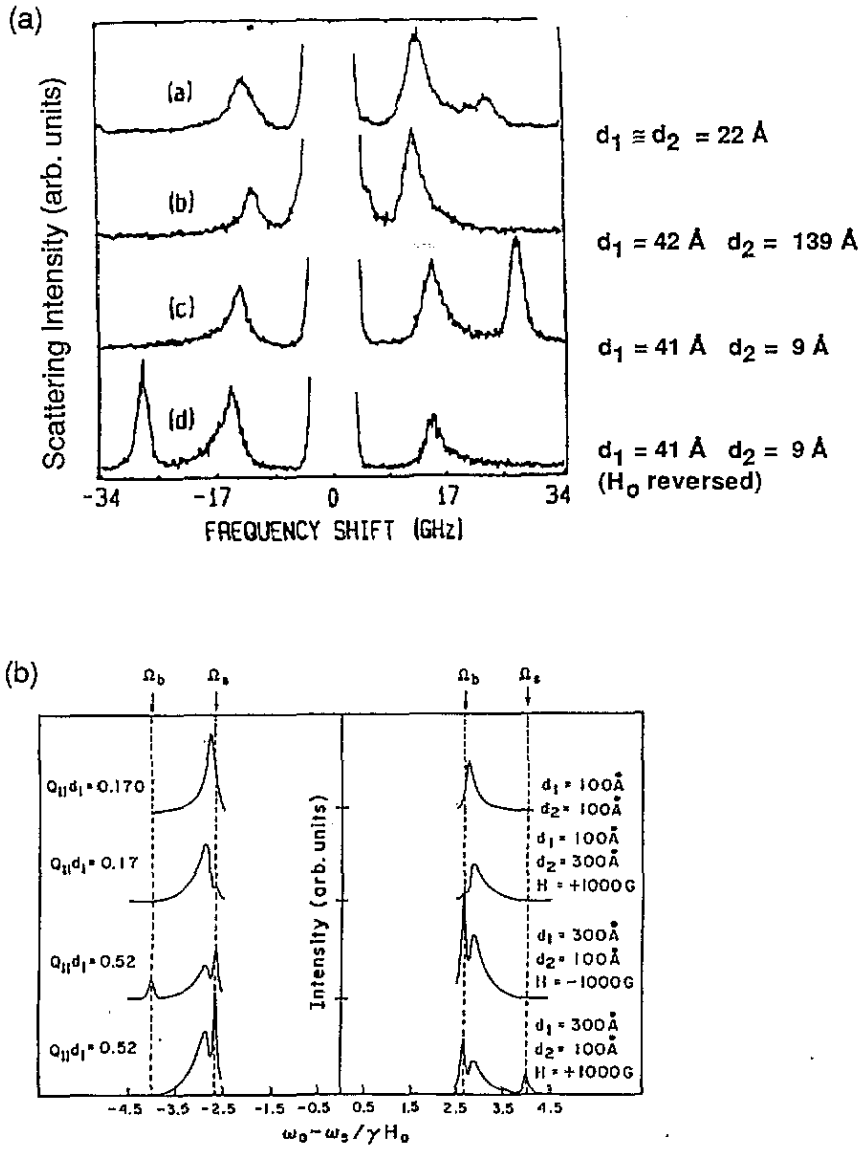

Figure 26. Theoretical and experimental Brillouin light scattering results for ferromagnetic/non-magnetic multilayers constructed with different magnetic/non-magnetic film thickness ratios. The low-frequency peaks show the scattering from the collective bulk bands and the high-frequency peak is the surface mode. The experimental results on Fe/Pd multilayers correspond very well to theory, with the surface peak only existing for $d_1 > d_2$. The surface mode switches sides as the applied field is reversed. (Theory, after [9]; experiment, B Hillebrands.)

thickness must be less than one tenth of the non-magnetic layer thickness, for example.

The transfer matrix method used above is especially useful for calculating the allowed modes of a finite multilayer. One proceeds essentially as we did in our discussion of surface waves by defining a magnetic potential outside each outside surface of the multilayer and applying the appropriate boundary conditions at both of these surfaces. Unlike our treatment of the semi-infinite stack, however, we must repeatedly apply the transfer matrix through

each layer of the multilayer in order to relate the coefficients of the magnetic potential at one outer surface to the coefficients at the other surface. This calculation can easily be done numerically, although diagrammatic methods are also available which allow one to perform the matrix multiplications fairly simply [97].

3.2.5. Spin waves in canted multilayers—effective medium theory. As described in section 2 of this article, the equilibrium orientations of the magnetizations of each film are determined by the competition between exchange interactions, interactions with the static applied field, and anisotropies. A very simple but interesting case occurs when the exchange interaction between the magnetic layers across non-magnetic spacer layers is antiferromagnetic, as discussed in section 2. In this case the Zeeman interaction tries to align the magnetizations of each film along the applied field, while the antiferromagnetic exchange interaction tries to align the magnetizations of neighbouring films antiparallel. For simplicity we assume that this competition results in a spin configuration such as that shown in figure 15(*a*).

We illustrate the basic features of this system with an example consisting of N ferromagnetic layers separated by $N-1$ non-magnetic layers. As shown in figure 15(*a*), the magnetizations of each magnetic layer are assumed to make an angle θ with the external applied field. The magnetizations of neighbouring magnetic layers are rotated from one another by the angle 2θ. As the field is increased, θ will become smaller and will eventually go to zero. The magnetizations of all layers will then be parallel. The field strength for which this occurs is [60]

$$H_0 = 4J_i/M \tag{66}$$

where M is the net magnetic moment in a film.

As remarked in section 3.2.3, the most prominent features of a Brillouin light scattering spectrum from a magnetic multilayer come from the surface mode and the small $q_\parallel L$ bulk modes. We can make a very simple argument for the frequency dependence of these modes as a function of θ in the following way. First let us consider the surface mode. The frequency of the surface mode for a multilayer with $N \gg 1$ was shown to be given in equation (33). The surface mode is characterized by an exponential decay of the spin wave's magnetic potential away from the outer surface of the multilayer. The decay length is in general very long in comparison to the size of a unit cell. This means that the surface wave is fairly insensitive to changes in the magnetization over distances comparable to the length of a unit cell and instead is affected by the average magnetic properties of several unit cells. Thus the frequency of a surface wave depends not on M_s but on the average magnetization.

The average magnetization for the magnetic layers in a unit cell is given by

$$M_{avg} = M_s \cos\theta. \tag{67}$$

The frequency of the surface wave for $\theta > 0$ should then be obtained simply by replacing M_s in equation (33) by M_{avg} [98]:

$$\Omega_s = \tfrac{1}{2}\left(H_0 + 4\pi M_s \cos\theta\right). \tag{68}$$

The frequency of the $q_\parallel L = 0$ mode is the ferromagnetic resonance frequency given by

$$\Omega_b = \sqrt{H_0(H_0 + 4\pi M_s)}. \tag{69}$$

By exactly the same arguments as those given above, the frequency of this bulk mode for $\theta > 0$ should also be given by replacing M_s by M_{avg}.

The validity of this approximation can be checked by comparison to an effective medium calculation which takes into account the magnetic fields in each film and solves the appropriate electromagnetic boundary condition problem. The effective medium approximation is a relatively simple approach which correctly gives the frequencies of the surface and $q_\parallel L = 0$ bulk modes [99–102].

The essence of the effective medium method is as follows. The dynamic response of each magnetic layer is written terms of the dipolar fields in each layer via the Landau–Lifshitz equations of motion. In terms of configuration shown in figure 15, this results in a set of equations for the motion of spins canted at an angle θ from the direction of the applied field and another set of spins canted at an angle $-\theta$ away from the applied field direction. These two sets of equations are coupled through the interlayer exchange interaction J_i and dipolar fields.

Next, an average fluctuating magnetization $\boldsymbol{m}$ is defined as the sum of the fluctuating magnetizations created by the two sets of spins. If we label the magnetizations of adjacent films as $\boldsymbol{m}^a$ and $\boldsymbol{m}^b$ respectively, then $\boldsymbol{m}$ is simply

$$\boldsymbol{m} = \tfrac{1}{2}(\boldsymbol{m}^a + \boldsymbol{m}^b).$$

Correspondingly, the equations of motion for $\boldsymbol{m}$ are the sum of the two sets of equations of motion. These are

$$m_x = \tfrac{1}{2}\Big[\chi_1 \cos^2\theta\big(h_x^a + h_x^b\big) + \chi_2 \cos\theta\big(h_y^a + h_y^b\big) + \chi_4 \sin\theta\cos\theta\big(h_x^a - h_z^b\big)\Big] \tag{70}$$

$$m_y = \tfrac{1}{2}\Big[-\chi_2\big(h_x^a + h_x^b\big)\cos\theta + \chi_3\big(h_y^a + h_y^b\big) + \chi_2 \sin\theta\big(h_z^a - h_z^b\big)\Big] \tag{71}$$

$$m_z = \tfrac{1}{2}\Big[\chi_4 \sin\theta\cos\theta\big(h_x^a - h_x^b\big) - \chi_5 \sin\theta\big(h_y^a - h_y^b\big) + \chi_4 \sin^2\theta\big(h_z^a + h_z^b\big)\Big] \tag{72}$$

where $\boldsymbol{h}^a$ are the dipolar fields acting on the set of spins canted by θ from the field direction and $\boldsymbol{h}^b$ are the dipolar fields acting on the set of spins canted by $-\theta$ from the field direction. The χ values are given by

$$\chi_1 = -\Big(2M_s H_e / H_0^2\Big)\Omega_+^2 / \big[(\omega/\gamma)^2 - \Omega_+^2\big] \tag{73}$$

$$\chi_2 = \mathrm{i}M_s(\omega/\gamma) / \big[(\omega/\gamma)^2 - \Omega_+^2\big] \tag{74}$$

$$\chi_3 = -\big(H_0/2H_e\big)M_s H_0 / \big[(\omega/\gamma)^2 - \Omega_+^2\big] \tag{75}$$

$$\chi_4 = -\big(\Omega_-/2H_e\big)M_s\Omega_- / \big[(\omega/\gamma)^2 - \Omega_-^2\big] \tag{76}$$

$$\chi_5 = \mathrm{i}M_s(\omega/\gamma) / \big[(\omega/\gamma)^2 - \Omega_-^2\big]. \tag{77}$$

The field H_e is the antiferromagnetic exchange field defined as $H_e = J_i/g\mu_B$. The magnetizations are canted for $H_0 < 2H_e$. We also include an easy-plane-type anisotropy field, H_a, which tends to align the spins in the xz plane. The poles of the χ values are given by

$$\Omega_+^2 = H_0\big(H_0 + H_a\cos\theta\big) \tag{78}$$

$$\Omega_-^2 = 2H_e H_a \sin^2\theta. \tag{79}$$

To bring equations (70)–(72) into the form of a susceptibility $\boldsymbol{m} = \boldsymbol{\chi} \cdot \boldsymbol{h}$ an appropriate average field $\boldsymbol{h}$ must be defined. This can be done in direct analogy to the definition of an average $\boldsymbol{m}$:

$$\boldsymbol{h} = \tfrac{1}{2}(\boldsymbol{h}^{\mathrm{a}} + \boldsymbol{h}^{\mathrm{b}}). \tag{80}$$

The magnetic fields must obey Maxwell's equations and satisfy electromagnetic boundary conditions at the interfaces between films. Thus the tangential fields $\boldsymbol{h}$ and normal fields $\boldsymbol{b}$ must be continuous from film to film. In the geometry of figure 23, this means that $h_x^{\mathrm{a}} = h_x^{\mathrm{b}}$ and $h_z^{\mathrm{a}} = h_z^{\mathrm{b}}$ but does *not* require $h_y^{\mathrm{a}} = h_y^{\mathrm{b}}$. In order to satisfy the continuity of normal b requirement, one defines a field $\boldsymbol{h}$ in the non-magnetic films and uses the equations of motion to eliminate the quantities $h_y^{\mathrm{a}} + h_y^{\mathrm{b}}$ which appear in equations (70)–(72).

An effective medium susceptibility can then be calculated using equations (70)–(72). The resulting susceptibility tensor has the form

$$\boldsymbol{\chi} = \begin{bmatrix} \chi_{xx} & \chi_{zy} & 0 \\ \chi_{yz} & \chi_{yy} & 0 \\ 0 & 0 & \chi_{zz} \end{bmatrix}. \tag{81}$$

The boundary conditions on normal fields $\boldsymbol{b}$ introduce 'filling factors' into the poles of the susceptibilities which shift the resonance frequencies according to the relative thicknesses of the magnetic and non-magnetic films. Canting, on the other hand, also shifts the resonance poles and leads to the existence of a χ_{zz} term that does not appear when the magnetizations are aligned parallel. The explicit results are somewhat lengthy and can be found in [98]. Instead, we show the results for the special case of the limit of vanishing non-magnetic layer thickness:

$$\boldsymbol{\chi} = \begin{bmatrix} \chi_1 & \chi_2 & 0 \\ -\chi_2 & \chi_3 & 0 \\ 0 & 0 & \chi_{zz} \end{bmatrix} \tag{82}$$

where

$$\chi_{zz} = -\left(\Omega_{\mathrm{d}}/2H_{\mathrm{e}}\right) M_{\mathrm{s}} \Omega_{\mathrm{d}} / \left[(\omega/\gamma)^2 - \Omega_{\mathrm{d}}^2\right]. \tag{83}$$

The pole Ω_{d} of the zz component goes to zero as the canting angle goes to zero:

$$\Omega_{\mathrm{d}} = \sin\theta \sqrt{2H_{\mathrm{e}}(H_{\mathrm{a}} + 4\pi M_{\mathrm{s}})}. \tag{84}$$

Note that in this limit the system is identical to a two-sublattice easy plane antiferromagnet. The results here differ from earlier treatments of the antiferromagnet in that we have consistently taken demagnetizing fields into account whereas previous treatments did not. The resonance frequency given by equation (84) therefore includes a demagnetization factor $4\pi M_{\mathrm{s}}$ which does not appear in earlier calculations.

The effective medium susceptibilities derived in this manner are very useful in that magnetostatic excitations for finite and semi-infinite multilayers can be calculated as in section 3.1.2 for the magnetostatic excitations in a corresponding uniform medium. The difference is that one uses the effective medium susceptibilities in place of the susceptibilities for a homogeneous material (equations (24)). This method has been used to study ferromagnetic and antiferromagnetic superlattices [102–104] as well as for structures with helical and conical magnetic ordering [105]. Also, since the effective medium

susceptibilities are considerably different from those for a uniform ferromagnetic, the dispersion relation also differs from equation (32) and the decay constant is modified. These relations become

$$1-(\kappa\mu_{yy}/q_{\|})^2+\left[(q_x/q_{\|})\mu_{xy}\right]^2+2(\kappa/q_{\|})\mu_{yy}\mathrm{cotan}(\kappa L)=0 \tag{85}$$

with

$$\kappa=\left[\frac{q_{\|}^2(\sin^2\varphi\,\mu_{xx}+\cos^2\,\varphi\mu_{zz})}{-\mu_{yy}}\right]^{1/2} \tag{86}$$

The permeability μ is defined as usual: $\mu=1+4\pi\chi$. The angle φ is defined between $q_{\|}$ and the z axis. Finally we remark that an effective medium calculation of the surface-mode frequency gives the same result as an expansion to first order in $q_{\|}L$ of the dispersion relation obtained using the transfer matrix method [101].

In figure 27 we compare the results of effective medium theory to the approximations of equations (68) and (69). The circles are the surface-mode frequencies of equation (68) and the squares are the bulk-mode frequencies given by equation (69) with the replacement for M_s. In this figure the frequencies of the spin-wave modes are shown as functions of the applied field strength.

The full curve is the result of the explicit multilayer calculation for the surface mode. The shaded area represents the bulk band obtained from this same calculation. The $q_{\|}L=0$ mode lies at the bottom edge of the bulk band. For $H_0>0.9$ kG, the magnetizations of the magnetic films are aligned parallel to the field. For fields less than this, magnetizations are turned away from the direction of the field by the angle θ. The frequencies of the surface mode and lowest bulk mode decrease with decreasing field and go to zero as H_0 goes to zero. There is clearly very good agreement between the multilayer calculation and the approximations of equations (68) and (69) using the averaged magnetization, M_{avg}.

The results of the multilayer calculation show several interesting features in the $\theta>0$ region for fields below 2 kG. Here there are two bands of bulk modes and two surface modes. This is a common feature of multilayers composed of antiparallel ferromagnetic films. The modes from the two bands cross at $H_0\simeq 1$ kG. The highest-frequency mode begins near 20 GHz for $H_0=0$ and goes to zero at $H_0=2$ kG. This is a surface mode and exists only in the $\theta>0$ region.

Recent experiments on Co/Ru and Py/Ru multilayers by Faßbender *et al* [106, 107] have confirmed this picture. Using Brillouin light scattering they measured the frequency of the surface mode as a function of the applied field for a series of multilayers with differing Ru layer thicknesses. In particular, the surface-mode frequency tended toward zero as the field was decreased, as shown in figure 27.

The effective medium treatment presented in this section is based on the assumptions of a uniformly canted structure and excitations which are long wavelength in nature. In the next section we explore an approximate treatment for shorter-wavelength modes which includes dynamic exchange interactions. While useful, this treatment is also an approximation. A complete treatment for spin waves in arbitrarily canted structures that treats exchange and dipole contributions exactly is presented in section 3.3.

3.2.6. Effects of dynamic exchange interactions. To conclude our introductory examination of spin waves in magnetic superlattices, we discuss some aspects of dynamic exchange coupling between spins. To begin we recall that all of our discussions up to this point were

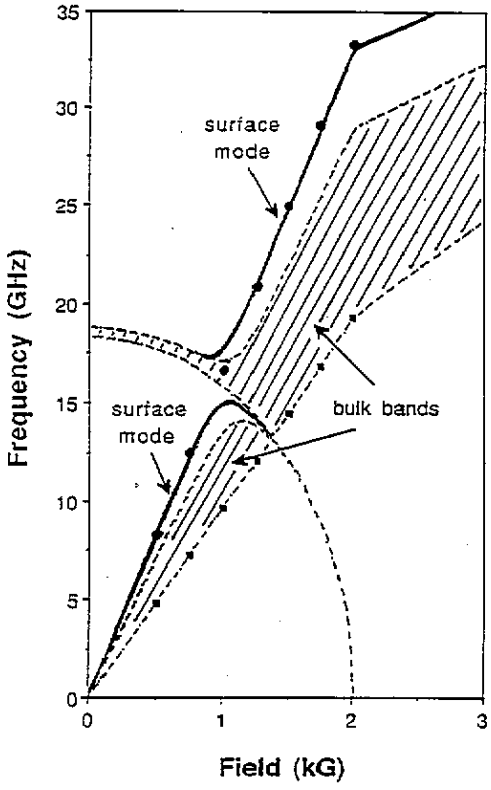

Figure 27. Spin wave frequencies for a canted structure. The frequencies of spin waves in a multilayer with antiferromagnetic interlayer coupling are shown as functions of the external applied field. In this example the magnetization is canted away from the applied field for fields below 2 kG. The magnetizations are aligned with the applied field for fields above 2 kG. The full curves are surface modes and the shaded areas are bulk bands calculated using effective medium theory. The circles and squares are calculated using the average magnetization per unit cell as in equation (68).

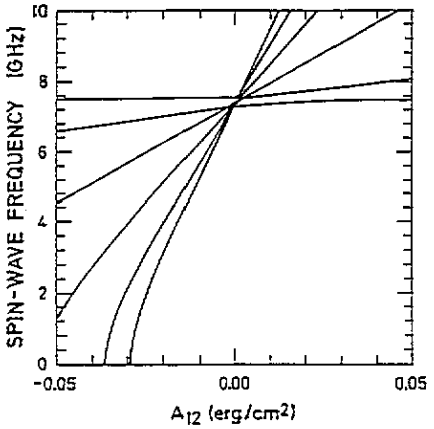

Figure 28. Spin-wave frequencies as functions of interlayer exchange. The lowest-frequency modes for a six-film multilayer are shown. Here positive A_{12} indicates ferromagnetic coupling and negative A_{12} antiferromagnetic coupling. The horizontal line is the surface wave and the others are bulk modes. The magnetizations are assumed to be parallel to the applied field. Note that the modes soften as A_{12} becomes more negative, indicating that the aligned state becomes unstable. (After [172].)

made under the assumption that the magnetic response of the spin systems could be described with a magnetic susceptibility χ that was independent of position as in equation (24). This is a valid description for spin-wave wavelengths which are very long in comparison to the lattice spacing, but the description breaks down for shorter wavelengths.

For short-wavelength excitations one needs to include terms in the Hamiltonian, or equivalently the equations of motion of equation (23), which take into account dynamic exchange interactions between neighbouring spins. One way of doing this is to include in the equations of motion an effective exchange field of the form [108]

$$h_{ex} = D\nabla^2 m \tag{87}$$

where D is the exchange stiffness constant and is proportional to the exchange constant of a Heisenberg spin model. The result of adding this term into the equations of motion is to introduce a spatial dispersion into the susceptibility.

Because of this, calculations which include both exchange and dipolar interactions can be quite complicated. The reason for this complication is that the exchange interaction is itself responsible for a family of pure exchange modes which are normal modes of a magnetic film. The dipolar interaction couples these modes and a superposition of exchange modes is required in order to satisfy the electromagnetic boundary conditions at each surface of a film [108]. In a multilayer, a superposition of exchange modes is required to satisfy the boundary conditions at each interface [109]. The special case of double layers was considered by Grünberg and co-workers [110]. We also note that most previous calculations employed Hoffman boundary conditions [111]. These conditions have been re-examined recently and small corrections have been shown to be necessary [112, 113].

Calculations which use an effective exchange field of the form given in equation (87) typically find approximate solutions to the problem by superposing six of the lower-energy exchange modes of each film at each interface. The calculation is somewhat involved and must be done numerically.

In a single thin ferromagnetic film, the spin waves gain an energy of the order of

$$D(q_{\parallel}^2 + q_y^2)^2 \tag{88}$$

where here we have written q_y to indicate the component of the spin wave's wavevector normal to the surface. For the surface mode and the $q_y = 0$ bulk mode, the energy increase is only $Dq_{\parallel}^2$, which is relatively small for typical light scattering experiments.

The main effect of including exchange interactions in the theory is to increase the energy of the bulk modes. For bulk modes, q_y is approximately given by

$$q_y = s\pi/d \tag{89}$$

where s is an integer and d is the thickness of the film. For Fe, D is of the order of 10^7 J cm^{-2}. For thin films of the order of 100 Å, even the $s = 1$ bulk modes have energies which are much larger than the surface mode. Therefore the lowest-frequency collective modes of a superlattice consisting of thin films will be composed of the surface modes of the individual thin films.

In a similar fashion, exchange coupling between the magnetic films of a multilayer will alter the frequencies of the collective modes. Interlayer exchange coupling, however is typically 100–1000 times smaller than intralayer exchange coupling. The collective surface mode will again remain largely unaffected, but the frequency of the collective bulk modes will change approximately according to

$$\Delta\omega \simeq \gamma J_i Q_y^2 = \gamma J_i (s\pi/L)^2 \tag{90}$$

where Q_y is the component of the Bloch wavevector along the axis of the multilayer and J_i is a measure of the strength of the interlayer exchange coupling. The height of the multilayer is L, as before. Note that the energies of the bulk modes decrease in the case of antiferromagnetic coupling where J_i is negative.

An example illustrating the effects of interlayer exchange coupling is shown in figure 28. Here the frequencies of the collective modes of a six-layer multilayer are shown as a function of interlayer exchange. Here A_{12} is a measure of J_i. The surface mode appears as the approximately horizontal full curve, and the energies of the remaining five bulk modes increase with increasing J_i. The larger Q_y is for a given mode, the more sensitive it will be to J_i. We note that the dependence of the bulk spin-wave energies on the ferromagnetic interlayer exchange has been demonstrated experimentally [109]. Oscillations in the sign of the interlayer exchange coupling as a function of non-magnetic layer thickness have also been extensively examined for Fe/Cr/Fe sandwiches [110] and Co/Ru superlattices [106].

3.3. Discrete model and phase transitions

In section 3.2.4 we encountered a simple example of how the dependence of spin-wave energies on the ground state configuration can signal a magnetic phase transition. In the example shown in figure 15 we see a transition between an antiparallel aligned state at zero applied field and a canted state for small field strengths, and finally a transition to a fully aligned state at larger fields. Each of these phase transitions is accompanied by the softening of a spin-wave mode.

In order to consider all of the phase transitions discussed in the second section of this article, we need a spin-wave theory that allows the spins to be able to lie at arbitrary angles to the direction of the applied field and also allows the angle of rotation to vary from layer to layer. A complete theory would also treat dipolar and exchange effects exactly and not resort to the long-wavelength approximations discussed in the previous sections. Such a model is by its nature discrete and uses the true effective fields at each lattice site.

We will present the general theory shortly, but first review by way of introduction what can be learned about some kinds of transition from a theory which assumes a simple uniform spin configuration. We will see, for example, that the surface phase transition in the Fe/Gd superlattice described in section 2 is accompanied by a softening of a surface spin-wave mode.

3.3.1. Surface phase transitions in semi-infinite superlattices. In section 2 we saw that the semi-infinite antiferromagnetically coupled Fe/Gd superlattice can display three different phases depending on the temperature and strength of the applied field (see figure 17). For a 13-layer Fe/five-layer Gd system at low temperatures and small applied fields, the Gd will prefer to align along the field direction. When the field is increased, and with Fe films at the surfaces, the system goes into a surface-twist phase as shown in figure 18. As discussed in section 2 the transition from the aligned Gd state to the surface-twist state begins with the outermost Fe spins. In contrast, an Fe/Gd superlattice constructed with Gd spins at the surface will undergo a transition from the aligned Gd phase to the twist phase than begins not at the surface, but in the bulk [59].

This disparate behaviour between Fe/Gd superlattices with Fe or Gd at the outer surface is also reflected in their respective spin-wave frequencies. We show this by calculating the spin-wave energies for each superlattice in the aligned state and observing the effects of increasing the applied field strength. In the following theory we neglect dipolar interactions and fields and include only nearest-neighbour exchange interactions [59].

With only exchange energies and the Zeeman energy due to the applied magnetic field, the equations of motion have the simple form

$$(\mathrm{d}/\mathrm{d}t)\boldsymbol{S}_n = \gamma \boldsymbol{S}_n \times \left(\boldsymbol{H}_0 + \sum_{\delta} J_{n,n+\delta} \boldsymbol{S}_{n+\delta} \right) \tag{91}$$

where $\boldsymbol{S}_n$ is a spin in layer n, δ is an index over nearest neighbours, and $J_{n,n+\delta}$ is the exchange interaction (in field units) between neighbouring layers of spins. A spatial and time dependence of the form $\exp[\mathrm{i}(\boldsymbol{q}_\parallel \boldsymbol{x}_\parallel - \omega t)]$ is assumed where $\boldsymbol{q}_\parallel$ is the component of the wave vector parallel to the interfaces.

A wave vector component perpendicular to the layers is also defined using the Bloch theorem. If the unit cell of the superlattice consists of a total of N Fe and Gd layers, then the spins in neighbouring cells are related by

$$\boldsymbol{S}_{n+N} = \boldsymbol{S}_n \exp(\pm \beta L) \tag{92}$$

where L is the length of the unit cell and β is the perpendicular component of the wave vector and is in general complex. Real β correspond to exponentially increasing or decreasing solutions and are associated with a surface wave. Imaginary β represent travelling waves associated with bulk spin waves. Substitution of these solutions into the equations of motion of equations (91) and linearizing results in two equations for the spins in each layer of a unit cell. The number of equations is reduced to one equation per spin layer by transforming to the variables $S^+ = S_x + iS_y$.

The equations of motion will be identical in form from one unit cell to the next except for the spins in the unit cell at the surface of the superlattice. In the bulk of the superlattice, the equations of motion for the spins in a unit cell are

$$\frac{\omega}{\gamma}\begin{bmatrix} S_1^+ \\ S_2^+ \\ \vdots \\ S_N^+ \end{bmatrix} = \begin{bmatrix} H_0 + s_N & DQS_1^z J_{1,2} & \cdots & 0 & \cdots & DQS_1^z J_{0,1}e^{-\beta L} \\ DQS_1^z J_{1,2} & H_0 + s_N & DQS_2^z J_{2,3} & \cdots & 0 & 0 \\ & & \vdots & & & \\ DQS_N^z J_{N,N+1}e^{\beta L} & \cdots & 0 & \cdots & DQS_N^z J_{N-1,N} & H_0 + s_{N-1} \end{bmatrix} \times \begin{bmatrix} S_1^+ \\ S_2^+ \\ \vdots \\ S_N^+ \end{bmatrix} \tag{93}$$

where $s_N = 4(S_N^z J_{0,1} + S_2^z J_{1,2})$ and $s_{N-1} = 4(S_{N-1}^z J_{N-1,N} + S_1^z J_{N,N+1})$, and where

$$DQ = -\Delta(q_\parallel) = -\cos(2q_x/a)\cos(2q_z/a) \tag{94}$$

with lattice constant a. A BCC lattice is assumed.

The equations of motion for spins in the surface unit cell are identical to equations (93) except that the first equation no longer contains terms coupling the outermost layer to the next cell. Thus the first equation is replaced by

$$(\omega/\gamma)S_1^+ = [H_0 + 4S_2^z J_{1,2}]S_1^+ - [\Delta(q_\parallel)S_1^z J_{1,2}]S_2^+. \tag{95}$$

There are then two unique sets of equations, one for the spins in the outermost unit cell and one for the spins in a unit cell in the bulk. The problem is then solved by choosing ω and β pairs that simultaneously satisfy both sets of equations for a given field H_0 and parallel wave vector $q_\parallel$. This is done numerically in a straightforward manner.

Results of this calculation for a superlattice composed of 13 layers of Fe and five layers of Gd per unit cell are shown in figures 29 and 30. In figure 29 $H_0 = 0$ and the spins are in the aligned state. The shaded areas are bulk modes. The circles show the surface mode for the superlattice with Fe at the surface and the squares show the surface mode for the superlattice with Gd spins at the surface. Note that the surface mode for the structure with Fe spins in the surface layer is separated from and lies below a bulk band. The surface mode and bulk band for the structure with Gd in the surface layer are degenerate with zero energy at $k = 0$.

The two bulk bands behave differently with respect to the applied field: the frequencies of the vertically shaded bulk band increase with increasing field and the frequencies of the horizontally shaded bulk band decrease with applied field. This is indicated by the arrows in figure 29. The surface spin-wave frequencies also depend quite differently on the applied field for each of the two structures. Again as shown by the arrows in figure 29, the surface-wave frequency for the Fe surface structure decreases with increasing field while the

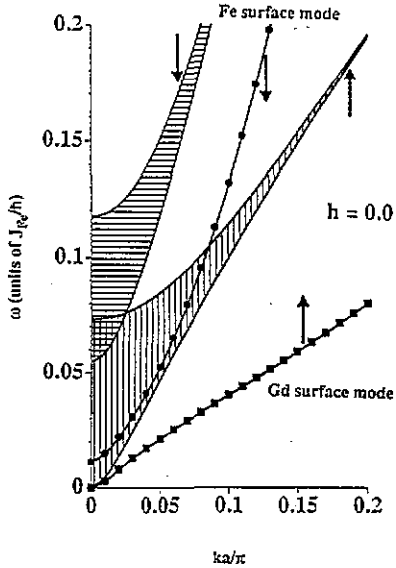

Figure 29. Dispersion relation for bulk and surface spin waves in a semi-infinite superlattice with unit cell 13 Fe/5 Gd. The applied field is zero. The arrows indicate the motion of the spin-wave dispersion curves with increasing field. The Fe surface mode occurs only for the system with Fe on the outside, while the Gd surface mode occurs only for the system with Gd on the outside. The bulk modes shown are those for an infinite sample and are thus independent of the surface. (After [59].)

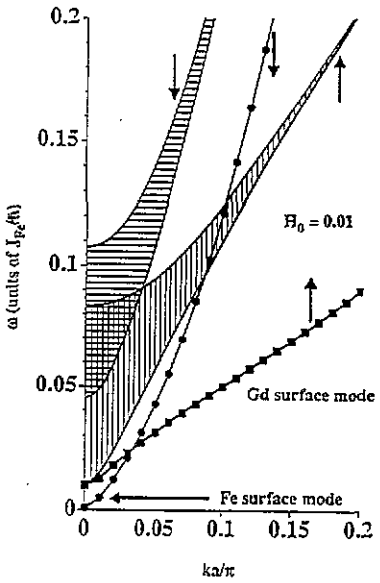

Figure 30. Dispersion relation for bulk and surface spin waves in a semi-infinite superlattice with unit cell 13 Fe/5 Gd. The applied field is $h = 0.01$, near the value needed to drive the lowest surface mode to zero frequency. The arrows indicate the motion of the spin-wave curves with increasing field. The Fe surface mode occurs only for the system with Fe on the outside, while the Gd surface mode occurs only for the system with Gd on the outside. The bulk modes shown are those for an infinite sample and are thus independent of the surface. (After [59].)

surface-wave frequency for the Gd surface structure increases with increasing field. This behaviour continues as the field is increased with the result for the Fe surface structure that the surface mode becomes soft at a finite field value.

Figure 30 shows the spin-wave modes for the same structures with $H_0 = 0.01 J_{Fe}$ where J_{Fe} is the exchange constant for bulk Fe in field units. This choice of field puts the Fe surface superlattice at the transition point between the aligned phase and the surface twist phase. The surface mode for the Fe surface structure has become soft for this field. The interesting point is that the softening of the surface mode signals a phase transition which nucleates at the surface. Examination of the ground state (see section 2) shows that the twist penetrates further into the bulk as the field is increased. It is interesting to note that the critical field for a transition to a state where all of the Fe and Gd spins are canted can in fact be as much as five times larger than the critical field for the transition to the surface-twist state.

3.4. Phase transitions in finite multilayers

The previous example illustrates some of the basic features of spin-wave dynamics near magnetic phase transitions. In particular we have seen that a phase transition is signalled by a mode softening. Some phase transitions occur because the environment of a surface spin is very different from that of a spin in the bulk and a softening of the surface mode is

a particularly sensitive indicator of these kinds of transitions. In order to study transitions between more complicated states using spin waves we must extend the dynamic theory to include arbitrary spin configurations [96].

A theory along the lines used for Fe/Gd can be constructed by first separating the spin variables into static and dynamic parts:

$$S_n(x_\parallel, t) = S_n + s_n \exp\left[i(q_\parallel \cdot x_\parallel - \omega t)\right]. \tag{96}$$

The equations of motion (equations (91)) are linearized by keeping only first-order terms in the components of s_n. The direction of S_n is found using the techniques of section 2. In general it is no longer possible to apply Bloch's theorem, and so one must solve the entire set of coupled equations for all magnetic layers in the multilayer. The set of equations can be put into eigenvalue form with frequencies ω as the eigenvalues. There are two equations for each layer resulting in a $2N$ by $2N$ matrix to be diagonalized. This of course places practical limits on the size of the multilayers we can describe with this theory.

It is also possible to extend the calculation to include dipolar coupling. This means adding to the equations of motion an effective field of the form

$$h_n^{\text{dip}}(x_\parallel, t) = (g\mu_B)^2 \sum_{n'} \sum_{x_\parallel'} \left[\frac{S_{n'}(x_\parallel', t)}{|r - r'|^3} - 3r \frac{r' \cdot S_{n'}(x_\parallel, t)}{|r - r'|^5} \right] \tag{97}$$

where r is the position vector to the spin at $(x_\parallel, n)$ and r' is the position vector to the spin at $(x_\parallel', n')$. As written the sums converge quite slowly, but techniques exist to put them into a rapidly convergent form [114].

A useful approximation can be derived for long-wavelength excitations. In this approximation the dipolar fields are written most conveniently in terms of their static and dynamic parts, defined as H_n and $h_n(q_\parallel)$, respectively. These are given by [96]

$$h_n(q_\parallel) = 2\pi q a (g\mu_B) \sum_{n'} \exp(-q_\parallel a|n - n'|) \times \begin{bmatrix} (q_z/q)^2 & i\ \text{sgn}(n-n')(q_z/q) & q_z q_x/q^2 \\ i\ \text{sgn}(n-n')q_z/q & -1 & i\ \text{sgn}(n-n')q_x/q \\ q_z q_x/q^2 & i\ \text{sgn}(n-n')q_x/q & (q_x/q)^2 \end{bmatrix} S_{n'} \tag{98}$$

and

$$H_n = 4\pi (g\mu_B) \begin{bmatrix} \frac{2}{3} & 0 & 0 \\ 0 & -1 & 0 \\ 0 & 0 & \frac{2}{3} \end{bmatrix} S_n. \tag{99}$$

The static term is nothing more than the local field acting on a spin within a ferromagnetic film. This approximation neglects, to some degree, the discrete nature of the lattice and assumes a demagnetizing field appropriate to a thick film. The errors involved are small however, even for quasi-two-dimensional films. Thus the variation in the dipolar field from layer to layer is reasonably well represented by this treatment.

Our first example is shown in figure 31. Here the lowest spin-wave energies are shown as functions of applied field for a multilayer constructed from ten magnetic layers. The parameters agree with those used in the effective medium theory to generate figure 27.

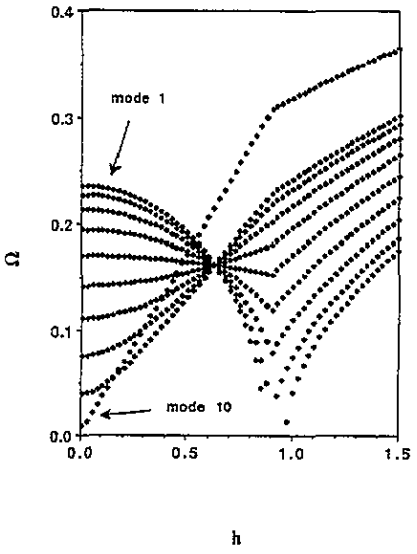

Figure 31. Spin-wave frequencies in the uniform canted state. The lowest spin-wave frequencies are shown as functions of applied field for a ten-film multilayer. The magnetizations are canted away from the field for $h < 1$ and parallel to the field for $h > 1$. Propagation is perpendicular to the field direction. The modes are numbered for future reference as shown. (After [96].)

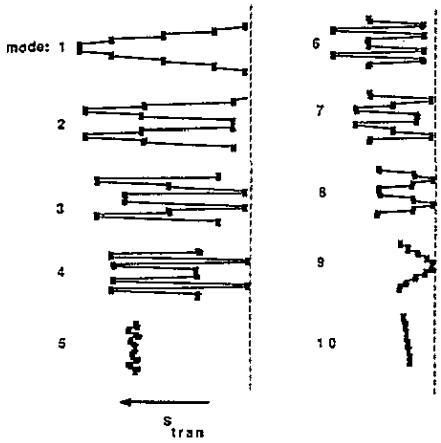

Figure 32. Mode profiles in the uniform canted state. The transverse magnitudes of spin fluctuations in the yx plane are shown for each of the ten lowest-energy modes shown in figure 31. Note the localization of mode 10 to one side of the multilayer. (After [96].)

A uniform ground state where θ is defined by equation (18) is also assumed in order to compare the two theories. The modes labelled 1 and 10 have the longest wavelengths and the frequencies of these modes agree well with the corresponding modes calculated with effective medium theory. The other modes shown in figure 31 are true bulk modes and are not correctly represented with effective medium theory. It is interesting to note that the bulk modes are degenerate in frequency at one field.

The transitions from aligned to canted spins can be seen in the frequencies of modes 1 and 10. The spins in adjacent films are canted for $0.9 > h > 0$. The energy of mode 1 decreases with increasing field until it finally becomes soft near $h = 0.9$ where the spins align in direction of the field. Note however that mode 1 actually becomes soft at a field smaller than $h = 0.9$. This is because we have used the wrong ground state spin configuration.

The mode amplitudes give information above the localization of spin waves. The amplitudes corresponding to the ten modes of figure 31 are shown in figure 32. The quantity plotted is the magnitude of the spin fluctuations in a plane transverse to the applied field, s_{trans} [115]. Mode 10, a surface mode, is significantly localized to an outer surface of the multilayer while the other modes are not.

A similar calculation using the correct ground state spin configuration (as determined by the methods described in section 2) is shown in figure 33. The transition to the aligned state occurs at $h = 0.9$ and mode 10 now softens at $h = 0.9$. There is now a great deal of mixing between all modes for fields less than 0.9. All the spin-wave amplitudes in the proper ground state are localized to the outer surfaces of the multilayer to some degree. Modes 3 and 6 are particularly strongly localized to the outer layers for this choice of field,

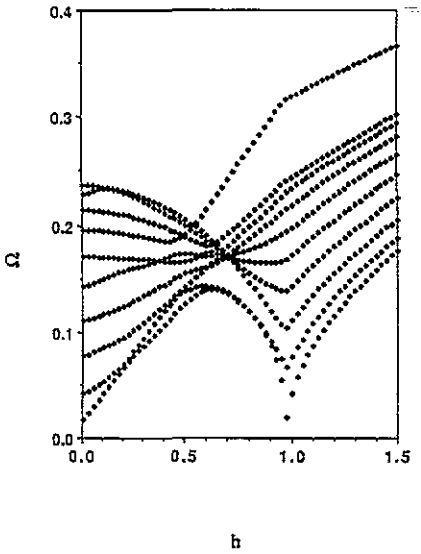

Figure 33. Finite-size effects. The correct ground state spin configurations were used in the calculation of the spin-wave frequencies. The frequencies are shown as functions of applied field for a ten-film multilayer. The ground state spin configurations resemble those shown in figure 15. The spins are aligned in the field direction for $h > 1$. Note the strong mixing of modes for $h < 1$. (After [96].)

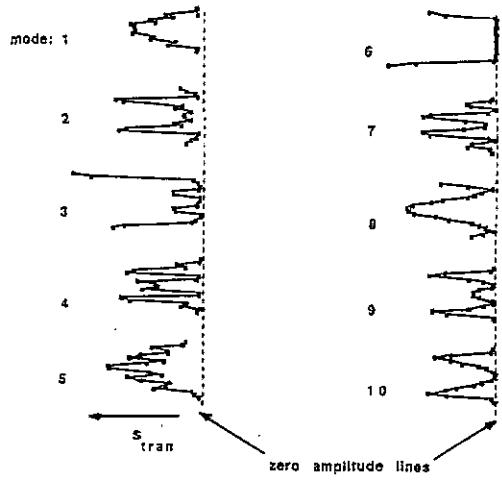

Figure 34. Localization of modes due to finite size. s_{tran} is shown at $h = 0.4$ for the modes of figure 33. The finite-size effects are due to the reduced exchange coupling experienced by the outermost films of the multilayer. This leads to a strong mixing of modes and the localization of several mode amplitudes to the outermost films of the multilayer. (After [96].)

as can be seen in figure 34 where the s_{tran} values are shown for the ten modes of figure 33.

4. Giant magnetoresistance in magnetic multilayers

4.1. Introduction

One of the most exciting and surprising properties of some of the new magnetic multilayers is the phenomenon of giant magnetoresistance. Here the resistivity of a multilayer structure can be changed by up to 60% (at room temperature) through the application of a magnetic field. This effect was originally discovered in Fe/Cr sandwiches [116] and multilayers [117] but has since been found in many other magnetic multilayers systems [47]. These include Co/Cu [48], Co/Ru [16], Ni/Ag [118] and Co/Au [119]. As we will see a key feature of the giant magnetoresistance is the change in the magnetic spin configuration as a function of applied field. Thus, as we saw in section 2, systems with some antiferromagnetic coupling are of particular interest.

The put the giant magnetoresistance effect into perspective, we first review the normal magnetoresistance effects in non-magnetic and magnetic metals [120]. For non-magnets, one generally finds a positive magnetoresistance effect in that the resistivity increases as an external field is increased. This increase is generally proportional to B^2. For magnetic materials one finds what is called the 'anisotropic magnetoresistance' effect where the resistivity of the metal depends weakly on the relative orientation of the magnetization and the current. The resistivity is generally largest when the magnetization and the current

are parallel ($\rho_\parallel$) and smallest when the magnetization and the current are perpendicular ($\rho_\perp$). For crystalline samples the resistivity tensor giving ρ in terms of the direction cosines of the magnetization with respect to the crystalline axis can be quite complicated. However for polycrystalline samples one finds the simple relationship that

$$\rho = \rho_\perp + \Delta\rho \cos^2\theta \tag{100}$$

where θ is the angle between the current and the magnetization; $\Delta\rho = \rho_\parallel - \rho_\perp$. For typical magnetic materials in use today $\Delta\rho$ is rather small. For example at room temperature $\Delta\rho/\rho_0$ is 0.2% for Fe, 2% for Ni and 3–4% for Permalloy.

In contrast to the above, the giant magnetoresistance effect measured in magnetic multilayers can be more than an order of magnitude larger. Also, the giant magnetoresistance effect is effectively independent of the relative orientation of the magnetic field with respect to the current, but depends on the relative orientation between magnetizations in neighbouring ferromagnetic films. As we will see, this orientational effect occurs because electrons with a specified spin in one Fe film can have a different spin direction when measured in a different Fe film with a different orientation for the magnetization.

In the Fe/Cr samples which were studied, there is an effective antiferromagnetic coupling between Fe films due to the intervening Cr films. As a result, the magnetic moments in neighbouring Fe films are antiparallel to each other in zero field. With a strong enough external field, the antiferromagnetic coupling may be overcome, and the magnetic moments of all the Fe films can be forced to lie in the same direction. A typical plot of the resistivity of an Fe/Cr/Fe sandwich structure is shown in figure 35. As can be seen, the resistivity is largest when the Fe moments are antiparallel and smallest at higher fields when the Fe moments are forced to be parallel.

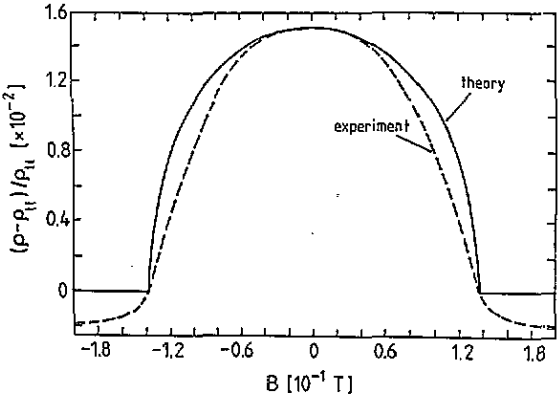

Figure 35. Percentage change in resistance as a function of applied field for a sandwich structure. The deviation of the experimental data from zero at high field is a measure of the size of the magnetoresistance anisotropy effect, neglected in the theory. (After [125].)

The experimental results on Fe/Cr multilayers [116, 117, 121] can be summarized as follows. (1) The resistivity is typically measured with the current flowing parallel to the interfaces. It is highest when the magnetic moments in neighbouring Fe films are antiparallel and smallest when they are parallel. (2) Multilayer structures with many thin Fe films have a much larger magnetoresistance effect (50% at low temperatures) than a single sandwich structure of Fe/Cr/Fe (3% at low temperatures). (3) Changing from room temperature to liquid He temperature increases the magnetoresistance by a factor of 2–3. (4) Experiments with the current flowing perpendicular [122] to the interfaces have shown significantly larger magnetoresistance effects than those with the currents flowing parallel to the interfaces, in agreement with theoretical calculations [123].

The physical mechanism responsible for the giant magnetoresistance effect is still not completely clear. It was originally suggested [117] that spin-dependent scattering at the interfaces was the dominant contribution. Such spin-dependent scattering is a well known phenomenon in magnetic metals [124]. For instance it is known that Cr impurities in Fe scatter up electrons 4–6 times more strongly than down electrons. Schematically one can understand this spin-dependent scattering in the following way. In most ferromagnetic metals the s electrons carry the majority of the current since the effective mass of the d electrons is quite large. The s bands are approximately parabolic but the d bands are exchange split as illustrated in figure 36. In a spin-conserving scattering process spin-up s electrons can scatter to the spin-up s or d bands. Similarly a spin-down electron scatters to the spin-down s or d bands. However as the density of states for the d bands is exchange split, the density of states at the Fermi level is different for spin-up and spin-down electrons leading to different scattering rates. Impurities can enhance this difference if the impurity states are spin split and have energies on one side which are at the Fermi level.

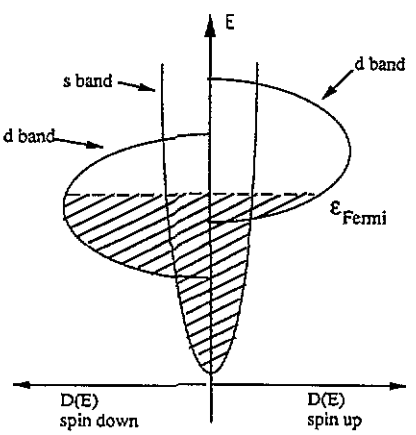

Figure 36. Schematic illustration of electronic density of states for Fe. The density of states for the up spins is shown on the right and for the down spins on the left. Note that the s band is approximately parabolic while the d bands are split. This results in a different density of states for the up and down electrons at the Fermi level.

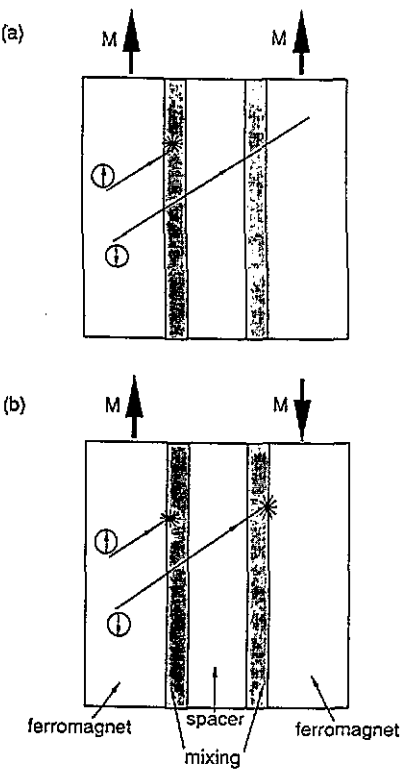

Figure 37. Spin-dependent scattering mechanism. (*a*) Possible particle motion for spin-up and spin-down electrons are shown when the magnetizations in neighbouring Fe films are parallel. A diffusive scattering event is indicated by a star. (*b*) The magnetizations are antiparallel, resulting in a larger net number of scattering events.

How such spin-dependent scattering could lead to the giant magnetoresistance is

illustrated in figure 37. In (*a*) we show typical particle motions for spin-up and spin-down electrons when the magnetizations in neighbouring Fe films are parallel. If a spin-up electron reaches an Fe/Cr interface it is likely to be diffusively scattered. On the other hand a spin-down electron can pass through one or more interfaces without being diffusively scattered. In (*b*) we examine the case where the magnetizations of the neighbouring Fe films are antiparallel. Here a spin-up electron approaches the Fe/Cr interface from the left as before and is diffusively scattered. A spin-down electron on the left passes through the left Fe/Cr interface but on reaching the right interface is locally a spin-up electron and thus has a high probability of being scattered. Comparing the two situations, we see that there are a larger number of scattering events when the Fe magnetizations are antiparallel than when they are parallel, and thus the resistivity is greater when the magnetizations are antiparallel. In this picture most of the spin-dependent scattering occurs at the interfaces because the largest mixing of Fe and Cr occurs at the interfaces.

The mechanism described above is clearly not the only possibility. Clearly some spin-dependent scattering can take place within the bulk of the ferromagnetic films as well. Also it is not clear that spin-dependent scattering asymmetries measured for low impurity concentrations appropriately represent the kind of scattering asymmetry to be found in an interface. These questions will be dealt with later in this section.

4.2. Theoretical model

We now turn to a simple theoretical model [125–127] which can describe the general features of the giant magnetoresistance. This model is an extension of the Sondheimer–Fuchs treatment of the resistivity of a thin film [128]. In this case it is assumed that the electron transport through the multilayer structure is governed by the semi-classical Boltzmann equation

$$-(e/m)(\boldsymbol{E}+\boldsymbol{v}\times\boldsymbol{B})\cdot\boldsymbol{\Delta}_{\boldsymbol{v}}f+\boldsymbol{v}\cdot\boldsymbol{\Delta}_{\boldsymbol{r}}f=-(f-f_0)/\tau \tag{101}$$

where f, the electron distribution function, depends on both position and velocity.

The geometry of our unit cell is presented in figure 38 which shows two films of Fe separated from a Cr film by a mixing region, m, on either side. Physically the mixing region represents the portion of the multilayer in which there are significant densities of both Fe and Cr. Experiments in the Fe/Cr system estimate that this mixing region can be on the order of 4 Å or larger. A static electric field is applied along the x axis parallel to the interfaces. A magnetic field is applied along the x axis in order to overcome the antiferromagnetic coupling between the Fe films. Note that the broken line separating regions C and D does not represent a true interface. Instead this is the point at which we take into account the change in quantization axis for the electron spin. Such a change is required because the Fe magnetizations in neighbouring films are not, in general, parallel to each other.

The conductivity of the structure is found from the electron distribution function which exists in the presence of the external electric field. In a perturbation expansion of this distribution function is given by the Fermi–Dirac distribution $f_0(v)$ plus corrections, $g(z, v)$ due to local scattering, surfaces and interfaces, and the electric field. The fact that the scattering rates depend on the position of the electron introduces the spatial dependence into the correction term. Thus we write

$$f^{\uparrow(\downarrow)}(z,v)=f_0^{\uparrow(\downarrow)}(v)+g^{\uparrow(\downarrow)}(z,v). \tag{102}$$

Here and in what follows the arrows refer to spin-up and spin-down electrons. For brevity we drop the functional dependence of g on z and v from now on. If we substitute equation (102)

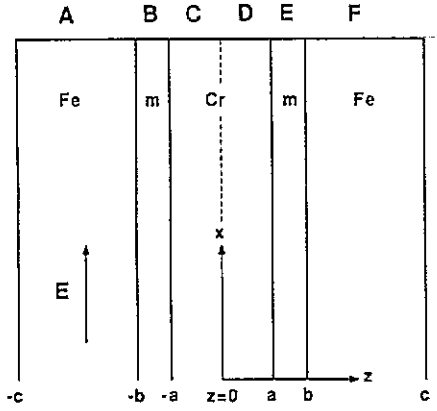

Figure 38. Geometry of the Fe/Cr/Fe sandwich including mixing regions. The centre of the structure is at $z = 0$, and the boundaries of the mixing region are at $z = \pm a$ and $z = \pm b$. An electric field is applied along the x axis, as shown. The $z = 0$ dotted line is an artificial boundary at which the change in quantization axis is introduced. (After [127].)

into the Boltzmann equation and retain only the linear terms in the perturbation we obtain

$$\partial g^{\uparrow(\downarrow)}/\partial z + g^{\uparrow(\downarrow)}/\tau^{\uparrow(\downarrow)} v_z = \left(eE/mv_z\right)\partial f_0/\partial v_x. \tag{103}$$

The term arising from $v \times B$ in the Boltzmann equation is also neglected since it is small. In this equation e is the electron charge, τ is a spin-dependent relaxation time, and m is the effective mass of the electron in each region. It is convenient to separate g into two parts: g_+ for electrons with positive v_z and g_- for electrons with negative v_z. Equation (103) is a simple first-order differential equation for g. The solution has the same form in each region. For example in region A one finds

$$g_{A\pm}^{\uparrow(\downarrow)} = \left(eE\tau^{\uparrow(\downarrow)}/m\right)\left(\partial f_0/\partial v_x\right)\left[1 + F_{A\pm}^{\uparrow(\downarrow)} \exp\left(-z/\tau^{\uparrow(\downarrow)} v_z\right)\right]. \tag{104}$$

Similar expressions hold for the other regions. The only unknowns at this point are the values of F appropriate for each region. These are functions of v and are found by using the boundary conditions at the interfaces between regions.

The boundary conditions connect the electron distribution functions at the interfaces. Since we assume that the Fermi–Dirac distribution function is spatially independent, only the g terms enter the boundary conditions. For example at the outer surface the distribution function g for an electron leaving the surface is equal to the distribution function for an electron of the same spin striking the surface multiplied by the probability p of a specular scattering event. Thus for the finite sandwich structure, where $z = \pm c$ represents the outer boundary, one obtains

$$g_{A+}^{\uparrow(\downarrow)} = p g_{A-}^{\uparrow(\downarrow)} \qquad \text{at } z = -c \tag{105}$$

$$g_{F-}^{\uparrow(\downarrow)} = p g_{F+}^{\uparrow(\downarrow)} \qquad \text{at } z = +c. \tag{106}$$

The infinitely extended superlattice structure may be treated by assuming perfectly reflecting surfaces at the outer boundaries (i.e. $p = 1$ in equations (105) and (106)) but setting the position of the interface at $\pm(c + b)/2$. The interior boundary conditions are derived in a similar manner. For example the distribution function for electrons leaving the interface at $z = b$ into region F depends on the probability of electrons in F hitting this interface and being reflected back into F, and the probability of electrons from region E being transmitted into region F. Thus one boundary condition at $z = b$ is given by

$$g_{F+}^{\uparrow(\downarrow)} = T^{\uparrow(\downarrow)} g_{E+}^{\uparrow(\downarrow)} + R^{\uparrow(\downarrow)} g_{F-}^{\uparrow(\downarrow)} \qquad \text{at } z = +b \tag{107}$$

where $T^{\uparrow}$ and $R^{\uparrow}$ are the transmission and reflection coefficients for an up spin. In principle these could be estimated using a free-electron-type model for each material by including contact potentials that arise from the differences in work functions for the different materials. An example of such a calculation is found in [129], but we will assume that the work functions for our materials are approximately the same. This is, in fact, reasonable for the Fe/Cr system. In this case we will assume that the transmission coefficient is always unity and the reflection coefficient is zero. The remaining boundary conditions that come from true interfaces are obtained in a similar manner. We find

$$g_{E-}^{\uparrow(\downarrow)} = T^{\uparrow(\downarrow)} g_{F-}^{\uparrow(\downarrow)} + R^{\uparrow(\downarrow)} g_{E+}^{\uparrow(\downarrow)} \qquad \text{at } z = +b \tag{108}$$

$$g_{E+}^{\uparrow(\downarrow)} = T^{\uparrow(\downarrow)} g_{D+}^{\uparrow(\downarrow)} + R^{\uparrow(\downarrow)} g_{E-}^{\uparrow(\downarrow)} \qquad \text{at } z = +a \tag{109}$$

$$g_{D-}^{\uparrow(\downarrow)} = T^{\uparrow(\downarrow)} g_{E-}^{\uparrow(\downarrow)} + R^{\uparrow(\downarrow)} g_{D+}^{\uparrow(\downarrow)} \qquad \text{at } z = +a \tag{110}$$

$$g_{C+}^{\uparrow(\downarrow)} = T^{\uparrow(\downarrow)} g_{B+}^{\uparrow(\downarrow)} + R^{\uparrow(\downarrow)} g_{C-}^{\uparrow(\downarrow)} \qquad \text{at } z = -a \tag{111}$$

$$g_{B-}^{\uparrow(\downarrow)} = T^{\uparrow(\downarrow)} g_{C-}^{\uparrow(\downarrow)} + R^{\uparrow(\downarrow)} g_{B+}^{\uparrow(\downarrow)} \qquad \text{at } z = -a \tag{112}$$

$$g_{B+}^{\uparrow(\downarrow)} = T^{\uparrow(\downarrow)} g_{A+}^{\uparrow(\downarrow)} + R^{\uparrow(\downarrow)} g_{B-}^{\uparrow(\downarrow)} \qquad \text{at } z = -b \tag{113}$$

$$g_{A-}^{\uparrow(\downarrow)} = T^{\uparrow(\downarrow)} g_{B-}^{\uparrow(\downarrow)} + R^{\uparrow(\downarrow)} g_{A+}^{\uparrow(\downarrow)} \qquad \text{at } z = -b. \tag{114}$$

The remaining boundary conditions occur at the artificial interface at $z = 0$. These change the description of the spin quantization axis from one Fe film to the proper quantization axis for the neighbouring Fe film. If the magnetizations of the two films make an angle θ with respect to each other, one obtains

$$g_{D+}^{\uparrow(\downarrow)} = \cos^2(\theta/2) g_{C+}^{\uparrow(\downarrow)} + \sin^2(\theta/2) g_{C+}^{\downarrow(\uparrow)} \qquad \text{at } z = 0 \tag{115}$$

$$g_{C-}^{\uparrow(\downarrow)} = \cos^2(\theta/2) g_{D-}^{\uparrow(\downarrow)} + \sin^2(\theta/2) g_{D-}^{\downarrow(\uparrow)} \qquad \text{at } z = 0. \tag{116}$$

The set of equations (105–(116) provide 24 conditions for the 24 unknown $F_{A\pm}^{\uparrow(\downarrow)}, \ldots, F_{F\pm}^{\uparrow(\downarrow)}$.

These are solved for numerically. There have also been treatments for structures with fewer interfaces where symmetry can be used to obtain analytic expressions for the unknown coefficients. Such treatments are helpful in that analytic forms for the magnetoresistivity can eventually be obtained [130].

Once all the values of F are known the values of g in each region can be evaluated and then the current density in each region is found by using the equation

$$J_x(z) = 2e\left(\frac{m}{\hbar}\right)^3 \int v_x g(v_z, z)\, \mathrm{d}^3 v. \tag{117}$$

The current in the whole structure may now be calculated by integrating the current density over z. This results in a relationship between the current and the applied electric field which gives the resistance of the structure. The external magnetic field changes the resistivity simply by changing the angle θ between neighbouring Fe films.

We comment briefly on the theoretical treatment. The original implementation of a Sondheimer–Fuchs-type calculation did not include a mixing region but instead introduced diffusive scattering parameters $D_{\downarrow}$ and $D_{\uparrow}$ to account for the asymmetry in scattering at a sharp Fe/Cr interface [125]. It was pointed out that in the limit where the mean free

path is much larger than the film thickness, the Sondheimer–Fuchs theory does not give a complete description because it allows electrons near the interface to propagate parallel to the interface for very long distances [131, 132]. This problem with the semi-classical method was reflected in the fact that the semi-classical model had difficulty in obtaining correct values for both the resistivity and the magnetoresistivity for the multilayer samples. Typically if the magnetoresistivity was correct the resistivity was somewhat (20–30%) too low. A proper quantum-mechanical-based treatment of the giant magnetoresistance effect does not have this problem as it treats both bulk scattering and interface scattering in the same fashion [132, 133]. Such a theory is however significantly more complicated.

Because of the simplicity of the semi-classical model various modifications have been introduced into the original treatment in order to correct its deficiencies. One such modification is the introduction of the mixing region as developed in [127] and reviewed here. Alternatively, the inclusion of anisotropic conductivity due to grain boundary scattering has also been shown to allow the Sondheimer–Fuchs-type models to calculate both resistivity and magnetoresistivity correctly [134]. Recently two real-space quantum calculations carried out with Kubo formalism have shown that the semi-classical model is effectively equivalent to the quantum model if the Fe/Cr interfaces are treated in the mixing region method as developed here [135, 136]. Thus with these improvements, the semi-classical model appears to provide a qualitative and quantitative understanding of the influence of the main parameters (mean free path to the electrons, thickness the magnetic and non-magnetic layers, asymmetry in scattering of up spins and down spins) on the magnetoresistance.

4.3. Behaviour of magnetoresistance as a function of structure

We now present some of the results of the semi-classical model and make comparisons to experimental data. We have already shown experimental and theoretical results for magnetoresistance as a function of applied field for a 120 Å Fe/10 Å Cr/120 Å Fe sandwich structure in figure 35. The variation of the angle θ between the magnetizations in neighbouring Fe films—necessary for calculating the magnetoresistance as a function of field—is found by minimizing the sum of the exchange Zeeman and anisotropy energies for this structure. The agreement between theory and experiment is quite reasonable. Other experimental work [121] has shown that the magnetoresistance varies as $\cos^2(\theta/2)$. This is a particularly interesting result in light of the fact that the transmission coefficients which arise due to the change in the quantization axis also vary as $\cos^2(\theta/2)$ as seen in equations (115) and (116). The full theoretical treatment developed here shows that the correct angular dependence is indeed quite close to a $\cos^2(\theta/2)$ law.

It is interesting to see how the magnetoresistance depends on the structure. In figure 39 we present the results of a calculation for magnetoresistance as a function of the thickness of the Cr spacer layer. Here we see a very rapid decrease of the magnetoresistance as the thickness of the Cr spacer layer is increased. The physical reason for this is clear. The mechanism outlined in figure 37 depends on a significant number of spin-down electrons being able to cross the spacer layer since it is the difference in the scattering of spin-down electrons for the parallel and antiparallel configurations which gives rise to the magnetoresistance. Since the mean free path in Cr is fairly short (10–20 Å) increasing the Cr thickness means that most electrons will be scattered inside the Cr layer and the magnetoresistance is significantly reduced.

In all cases we see that the superlattice has a significantly larger magnetoresistance than the single sandwich structure. The reason for this is that we have assumed completely diffusive scattering at the outer boundaries of the sandwich. This increases spin-independent

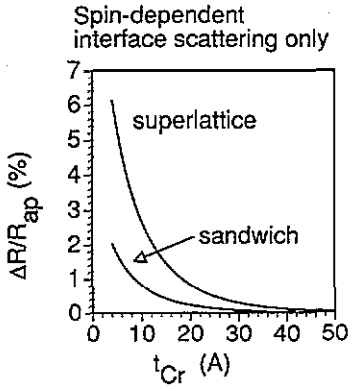

Figure 39. Magnetoresistance as a function of Cr film thickness. The magnetoresistance decreases rapidly with increasing Cr film thickness for both the simple sandwich structure and the superlattice. The parameters for the calculation are $\lambda_{Fe} = 40$ Å, $\alpha_{Fe} = 1$, $t_{Fe} = 15$ Å, $\lambda_{mix} = 18$ Å, $\alpha_{mix} = 0.217$, $t_{mix} = 4$ Å, $\lambda_{Cr} = 20$ Å, $\alpha_{Cr} = 1$. The mean free paths λ refer to the average value which includes both spin-up and spin-down electrons. $\alpha = \rho\downarrow/\rho\uparrow$ gives the scattering asymmetry for each region.

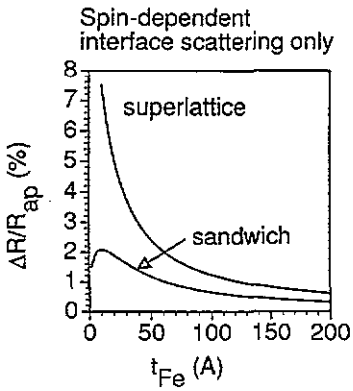

Figure 40. Magnetoresistance as a function of Fe film thickness for spin-dependent interface scattering. Increasing the Fe film thickness merely increases the number of scattering events within the films, thus increasing the total resistance. The magnetoresistance is here determined by spin-dependent interface scattering and so the net effect decreases with increasing Fe thickness. The parameters for the calculation are $\lambda_{Fe} = 40$ Å, $\alpha_{Fe} = 1$, $\lambda_{mix} = 18$ Å, $\alpha_{mix} = 0.217$, $t_{mix} = 4$ Å, $\lambda_{Cr} = 20$ Å, $\alpha_{Cr} = 1$, $t_{Cr} = 4$ Å.

scattering and lowers the magnetoresistance. This seems to be in accord with current experimental results. However it would be interesting to try various experimental treatments to make the outer surfaces of the sandwich structure have a larger amount of specular scattering. Then, in principle, one could obtain quite large magnetoresistances in the sandwich as well as in the superlattice.

The results for the magnetoresistance as a function of the magnetic layer thickness are more complicated. In this case the results depend strongly on whether the magnetoresistance is due to spin-dependent *bulk* scattering or spin-dependent *interface* scattering. If one has pure spin-dependent interface scattering then increasing the Fe thickness simply results in more of the electrons being scattered within the Fe films. Thus the dominant contribution to the resistivity comes from scattering which does not involve the electrons crossing from one Fe film to another. In this case the magnetoresistance monotonically decreases as the thickness of the Fe layer is increased. This can be seen in figure 40. In contrast, for primarily spin-dependent bulk scattering, increasing the Fe thickness initially provides more opportunities for spin-dependent scattering. Thus in very thin Fe layers most of the scattering occurs within the Cr and the magnetoresistivity is low. As the Fe becomes thicker the mechanism outlined in figure 37 becomes possible and the magnetoresistivity increases. Finally as the Fe thickness becomes significantly larger than a mean free path most of the scattering is within one Fe film and the magnetoresistance again decreases. This explains the behaviour of the magnetoresistance as a function of t_{Fe} seen in figure 41.

In figure 42 we explore how the magnetoresistance depends on the number n of unit cells and on the mean free path in the ferromagnet. The structure is $(Fe/Cr)_n/Fe$. This calculation is performed for the case where the scattering is primarily interface scattering. As the mean free path is increased the number of spin-independent scattering events is decreased while the number of spin-dependent scattering events is about the same. Thus the magnetoresistance increases. Also, as n is increased the effect of the spin-dependent

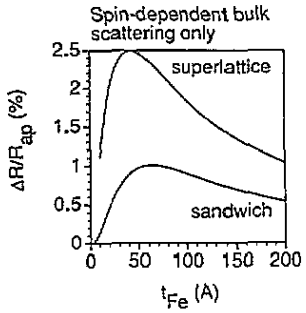

Figure 41. Magnetoresistance as a function of Fe film thickness for spin-dependent bulk scattering. Initially increasing the Fe film thickness increases the net magnetoresistance effect by increasing the probability of spin-dependent scattering. When the Fe thickness becomes much larger than the mean free path in Fe, the magnetoresistance decreases again with increasing Fe thickness. The parameters for the calculation are $\lambda_{Fe} = 40$ Å, $\alpha_{Fe} = 0.333$, $\lambda_{mix} = 18$ Å, $\alpha_{mix} = 1$, $t_{mix} = 4$ Å, $\lambda_{Cr} = 20$ Å, $\alpha_{Cr} = 1$, $t_{Cr} = 4$ Å. The mean free paths refer to the average value which includes both spin-up and spin-down electrons.

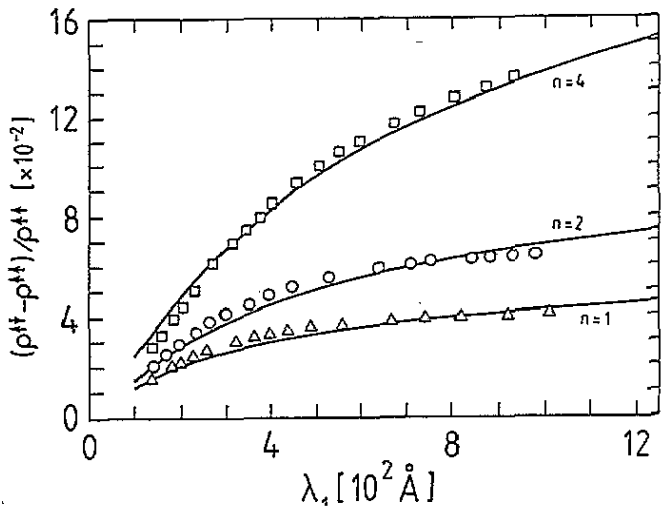

Figure 42. Magnetoresistance as a function of mean free path for different size multilayers. The experimental results are given by the symbols and the theory is given by the full curves. The magnetoresistance increases with increasing mean free path in Fe ($\lambda_\uparrow$) and with increasing number of magnetic films. (After [126].)

diffusive scattering at the outer layers is reduced and the magnetoresistance is also increased.

4.4. Bulk and interface spin-dependent scattering and the influence of impurities at the interfaces

There has been a fair amount of controversy about whether the spin-dependent scattering found in experiments is primarily interface or bulk scattering. Theoretical calculations [127, 132] (which show excellent agreement with experimental results) for the Fe/Cr system indicate that about 65–75% of the magnetoresistance arises from scattering at interfaces. In contrast, $Ni_{80}Fe_{20}$/Cu multilayer structures have been analysed within a picture where bulk scattering is dominant [134]. (This requires a scattering asymmetry $\rho_\downarrow/\rho_\uparrow = 1/15$–$1/20$ which is apparently reasonable for Permalloy.) Other models for Co/Cu superlattices also invoke bulk spin-dependent scattering [137]. However a recent experiment reports dramatic enhancement of magnetoresistance in $Ni_{81}Fe_{19}$/Cu multilayers by the addition of thin Co layers at the interfaces, indicating that interface effects may be very important in these systems [138]. It is fair to say that the general situation is not completely resolved at this time, and some material combinations may display primarily interface scattering while others seem to have a large component of bulk scattering as well. It is expected that careful comparisons of experimental data to curves such as figures 39–41 should be able to establish whether bulk or interface scattering is dominant in a particular sample. Some work in this direction has already been completed [134].

The question of whether the magnetoresistance is due to bulk or interface spin-dependent scattering impacts on another topic, the role of interface roughness in giant magnetoresistance [139–142]. Clearly if the magnetoresistance is primarily due to bulk spin-dependent scattering then increasing interface roughness would increase the resistivity in general and the magnetoresistivity would be reduced. In contrast, interfacial spin-dependent scattering might reasonably be expected to increase with interfacial disorder and the magnetoresistivity should increase. Such a result is in qualitative agreement with both quantum models, where the giant magnetoresistance is a function of spin-dependent random potentials at the interface, and semi-classical models, where more roughness could result in a larger mixing region.

There are some experimental results indicating that the Fe/Cr system shows increased magnetoresistance with increased interfacial roughness. In one study [139] the interfacial roughness was inferred from x-ray diffraction measurements on sputtered Fe/Cr superlattices. In particular, a larger intensity of the first Bragg peak arising from the superlattice structure was used to indicate a system with less interfacial roughness. Increasing background Ar pressure or decreasing Fe sputtering power generally resulted in rougher interfaces and an increase in magnetoresistance.

An interesting attempt to confirm the picture of spin-dependent scattering as the origin of the giant magnetoresistance effect involved the introduction of impurities at the Fe/Cr interfaces [143]. These additional impurities have known asymmetries for scattering of spin-up and spin-down electrons. If the spin-dependent scattering mechanism is correct, then when the impurities have the same asymmetric scattering as Cr in Fe there should only be a small change in the magnetoresistance as a function of impurity content. In contrast if the scattering asymmetry of the impurity is opposite to Cr in Fe the magnetoresistance should be significantly decreased. Of course such a picture assumes that scattering asymmetries measured at low concentrations of impurities in bulk Fe have some relevance to the high-concentration region found at the interfaces.

Many different impurity elements have now been added to the Fe/Cr interface region in experimental studies [143, 144]. The scattering asymmetry parameter $\alpha = \rho_\downarrow/\rho_\uparrow$ for these elements as dilute impurities in Fe is given in table 1. Table 1 also summarizes the change in the magnetoresistance when these elements are introduced at the Fe/Cr interface. Despite the scatter in the asymmetry parameter, impurities which have values of α which are close to those found for Cr do not degrade the magnetoresistance significantly. Impurities which have α significantly larger than those found for Cr (i.e. weak asymmetry for $0.5 < \alpha < 1$ or scattering asymmetry opposite to that of Cr for $\alpha > 1$) result in significant reduction of the magnetoresistance. Despite these intial indications that the scattering asymmetry found in the previously measured values of α is important, we emphasize that the physical situation in these experiments is quite complex and much work remains to be done.

The theoretical development presented in this section can be applied in a straightforward manner to the calculation of magnetoresistance with impurities in the 'mixing region'. In this case one can start an estimation for the scattering asymmetry α in the mixing region by using Matheson's rule to find the total resistivity due to scattering from Cr and from the impurity for spin-up electrons. This is also performed separately for spin-down electrons and then the ratio $\rho_\downarrow/\rho_\uparrow$ is formed. The effect of the impurities on the mean free path in the mixing region may also be included. Theoretical calculations and experimental results for the magnetoresistance as a function of impurity content are shown in figure 43. The behaviour of Al and Mn as impurities are clearly quite different, with Al causing a very rapid decrease in the magnetoresistance. Increasing Mn also causes a decrease, but it is essentially the same decrease that one observes when the Cr layer thickness is increased.

Table 1.

Impurity element	$\alpha = \rho_\downarrow/\rho_\uparrow$	Effect on magnetoresistance	Reference
V	0.12–0.13	slow decrease	[143, 144]
Cr	0.17–0.37	slow decrease	[143, 144]
Mn	0.09–0.17	slow decrease	[143, 144]
Mo	0.21	slow decrease	[144]
Ru	0.37	slow decrease	[144]
Ti	0.25–0.66	moderate decrease	[144]
Al	8.6	rapid decrease	[143]
Ir	9.0	rapid decrease	[143]
Ge	6.2	rapid decrease	[143]

This behaviour is consistent with the scattering asymmetries of Al and Mn impurities in bulk Fe.

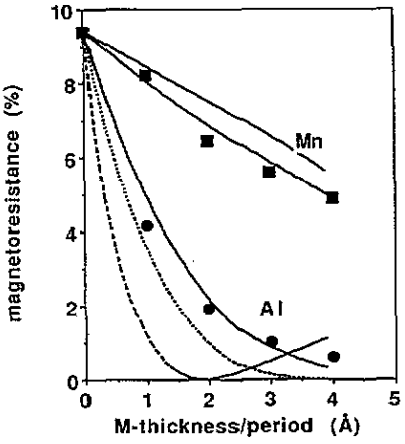

Figure 43. Magnetoresistance of Fe/Cr multilayers as a function of the thickness of impurity layer added at the Fe/Cr interface. Circles and squares indicate experimental data from [143]. Full and broken curves are theoretical calculations from [127]. A clear difference is seen between the results for Mn (which has α close to the value for Cr) and Al (which has an α very different from that of Cr). The different theoretical curves are based on the range of assumed values for α for each impurity.

4.5. Additional systems and theoretical treatments

The examples considered earlier dealt with compounds where the antiparallel arrangement was introduced by some effective antiferromagnetic exchange between ferromagnetic films. The giant magnetoresistance does not seem to depend on the antiferromagnetic exchange, but rather simply on the possibility of changing from antiparallel orientation to parallel orientation. A number of systems have been developed which show giant magnetoresistance but without antiferromagnetic exchange between the ferromagnetic films. These include sandwich structures where the antiparallel alignment is obtained by making the coercive fields for the two different ferromagnetic films different [126, 145] and structures which are fabricated in thin stripes so that dipolar fields cause an antiparallel orientation [146].

A particularly interesting structure where antiparallel alignment can be obtained without antiferromagnetic coupling between the ferromagnetic films is the so-called spin valve. Here one has a sandwich where one ferromagnetic film, say the lower film, is exchange coupled to an antiferromagnet [147–149]. In this case application of a weak external field can readily change the direction of the magnetization for the upper ferromagnetic film, but the magnetization of the lower ferromagnet is held antiparallel to the field by the coupling to

the antiferromagnet. At higher fields the magnetization of the lower film is also forced to lie in the direction of the field, resulting in parallel alignment.

A number of microscopic theoretical approaches have also been employed to understand the giant magnetoresistance in layered structures. These have concentrated on viewing the system directly from an electronic band structure calculation [150–153]. Calculations have been performed within the coherent potential approximation [151, 152]. One calculation using the tight-binding method explicitly included roughness effects at the interfaces [153].

Finally we note that giant magnetoresistance is not limited to layered structures but has also been found in granular thin films, particularly in Co–Ag [154–156] and Co–Cu systems [157]. Giant magnetoresistance in magnetic granular films has also been discussed theoretically [158]. The origin of giant magnetoresistance in these alloys is also attributed to spin-dependent scattering. Here it is assumed that at low fields the magnetizations of small particles of Co are randomly oriented and that at high fields the magnetizations are all aligned with the external field. Thus one has a similar orientational effect as in the multilayer structure and the same mechanism can be used in both cases.

5. Conclusion

We have seen that the physics of magnetic multilayers and superlattices is clearly a rich and varied field, with questions to challenge the experimentalist and theorist alike. Our presentation has been a survey of only some of the many interesting questions, and has out of necessity completely ignored a number of equally fascinating phenomena.

One area of intense research has been concerned with how intrinsic magnetic properties are effected by superlattice structures. Therefore questions about magnetic 'dead' layers, enhanced magnetic moments, and contributions to anisotropies from elastic strains and interface effects have been addressed using a variety of experimental techniques and theoretical band structure calculations [12, 159–162]. The formation of anisotropies in multilayer structures is particularly fascinating, since it appears possible to control the type and orientation of the anisotropy with the superlattice construction [163, 164]. Anisotropy can also be responsible for magnetic phase transitions. For example an easy axis perpendicular to the film can lead to a phase transition involving a reorientation of spin direction from parallel to the film plane to perpendicular. This has been examined both theoretically [165] and experimentally [166].

In order to complete our survey of this field, we cannot ignore the multitude of exciting possible applications for many of the phenomena we have described. Some of the most promising applications involve the giant magnetoresistance effect described in section 4. The order of magnitude improvement in sensitivity over conventional magnetoresistance makes this phenomenon attractive for a surprisingly large class of device applications. Among the various devices which use magnetoresistance sensors are [167, 168] pressure sensitive switches such as those used in electronic keyboards, magnetic read-out heads, magnetic sensors such as those used in traffic control, and novel magnetic data storage devices [169].

The magnetization of magnetic materials is also an often used property for other classes of applications. Long-lasting rewritable data storage materials are usually magnetic. New materials constructed from multilayers composed of thin magnetic films allow for much higher storage densities than possible with conventional magnetic media [170]. These are particularly well suited for optical writing and reading technologies which use the optical Kerr rotation effect [171]. There are obvious advantages to using a multilayer construction, since this allows one to tailor the material properties to the specific device need. Some

of the most relevant magnetic properties that can be controlled through the superlattice geometry are anisotropies and interlayer exchange. We have seen how simply modifying the interlayer exchange can lead to radically different thermodynamic behaviour, an aspect that is critical in the optical writing of data onto magnetic media.

Finally we comment on applications involving the optical properties of magnetic superlattices. Superlattices constructed from antiferromagnetic materials are of possible interest to communications and signal processing technologies for devices that work at wavelengths in the infrared [88]. The optical response of antiferromagnetic multilayers and superlattices at these wavelengths is determined by their dynamic magnetic response. Not only are linear response characteristics important, but their non-linear response is also of great interest [88]. Potentially useful features include a variety of different phenomena such as harmonic generation and bistable transmission.

The short description given here of possible applications is by no means complete, nor is it appropriate to go too deeply into this subject here. We have instead presented only an outline of some of the more interesting possibilities currently under consideration or even development, and are certain that the future will bring even more.

Acknowledgments

This work was supported by the US Army Research Office through grant DAAL0391-G-0229. Much of this work has grown out of collaborations and stimulating discussions with many people. We would especially like to than N S Almeida, J Barnas, Ph Bauer, P Baumgart, A S Carriço, K Cherifi, M G Cottam, C Dufour, J Fassbender, P Grünberg, G Güntherodt, B Hillebrands, B L Johnson, J Kwo J G LePage, D L Mills, Ph Mangin, G Marchal, F C Nörtemann, T S Rahman, M Sajieddine, D R Tilley and W Zinn.

References

[1] Morishita T, Togami Y and Tsushima K 1985 *J. Phys. Soc. Japan* **54** 37
[2] Tsunashima S, Ichikawa T, Nawate M and Uchiyama S 1988 *J. Physique Coll.* **49** C8 1803
[3] Weller D, Alvarado S F, Gudat W, Schroder K and Campagna M 1985 *Phys. Rev. Lett.* **54** 1555
[4] Moorjani K and Coey J M D 1984 *Magnetic Glasses* (New York: Elsevier) ch 6
[5] Pappas D P, Kämper P, Miller B P, Hopster H, Fowler D E, Brundle C R, Luntz A C and Shen Z X 1991 *Phys. Rev. Lett.* **66** 504
[6] Erickson R P and Mills D L 1991 *Phys. Rev.* B **44** 11 825
[7] Kwo J, Hong M, Di Salvo F J, Waszczak J V and Majkrzak C F 1987 *Phys. Rev.* B **35** 7925
Majkrzak C F, Cable J W, Kwo J, Hong M, McWhan D B, Yafet Y, Waszczak J V and Vettier C 1986 *Phys. Rev. Lett.* **56** 2700
[8] Kwo J, Gyorgy E M, McWhan D B, Hong M, Di Salvo F J, Vettier C and Bower J E 1985 *Phys. Rev. Lett.* **55** 1402
[9] Camley R E, Rahman T S and Mills D L 1983 *Phys. Rev.* B **27** 261
[10] Grimsditch M, Kahn M R, Kueny A and Schuller I K 1983 *Phys. Rev. Lett.* **51** 498
[11] Grünberg P and Mika K 1983 *Phys. Rev.* B **27** 2955
[12] Shinjo T 1991 *Surf. Sci. Rep.* **12** 51
[13] Majkrzak C F, Kwo J, Hong M, Yafet Y, Gibbs Doon, Chien C L and Bohr J 1991 *Adv. Phys.* **40** 99
[14] Qiu Z Q, Pearson J and Bader S 1992 *Mod. Phys. Lett.* **6** 839
[15] Senda M and Nagai Y 1989 *J. Appl. Phys.* **65** 3157
Dufour C, Bruson A and Marchal G 1991 *J. Magn. Magn. Mater.* **93** 545
[16] Parkin S S P, More N and Roche K P 1990 *Phys. Rev. Lett.* **64** 2304
[17] Nagai Y and Senda M 1988 *J. Appl. Phys.* **64** 4108
Kim C, Quadri S B and Yu H Y 1990 *J. Vac. Sci. Technol.* **8** 1407

[18] Fujimori H, Kamiguchi Y and Hayakawa Y 1990 *J. Appl. Phys.* **67** 5716
[19] Kamiguchi Y, Hayakawa Y and Fujimori H 1989 *Appl. Phys. Lett.* **55** 1918
[20] Cherifi K, Dufour C, Bauer Ph, Marchal G and Mangin Ph 1991 *Phys. Rev.* B **44** 7733
[21] Cherifi K, Dufour C, Marchal G, Mangin Ph and Hubsch J 1992 *J. Magn. Magn. Mater.* **104–107** 1833
[22] Fujimori H, Kamiguchi Y, Hayakawa Y and Takanashi K 1992 *MRS Symp. Proc.* **231** 125
[23] Landes J, Sauer Ch, Kabius B and Zinn W 1991 *Phys. Rev.* B **44** 8342
[24] Bauer Ph, Sajieddine M, Dufour C, Cherifi K, Marchal G and Mangin Ph 1991 *Europhys. Lett.* **16** 307
[25] Camley R E, Kwo J, Hong M and Chien C L 1990 *Phys. Rev. Lett.* **64** 2703
[26] Majkrzak C F, Gibbs Doon, Böni P, Goldman Alan I, Kwo J, Hong K, Hsieh T C, Flemming R M, McWhan D B, Yafet Y, Cable J W, Bohr J, Grimm H and Chien C L 1988 *J. Appl. Phys.* **63** 3447
[27] Grünberg P, Schreiber R, Pang Y, Brodsky M B and Sowers H 1986 *Phys. Rev. Lett.* **57** 2442
[28] Salamon M B, Sinha S, Rhyne J J, Cunningham J E, Erwin R W, Borchers J and Flynn C P 1986 *Phys. Rev. Lett.* **56** 259
Rhyne J J, Borchers J, Sinha S, Salamon M B, Du R and Flynn C P 1987 *J. Appl. Phys.* **61** 4043
[29] Erwin R W, Rhynne J J, Salamon M B, Borchers J, Sinha S, Du R, Cunningham J E and Flynn C P 1987 *Phys. Rev.* B **35** 6808
[30] Ramos C A, Lederman D, King A R, Jaccarino V 1990 *Phys. Rev. Lett.* **65** 2913
[31] Lind D M, Berry S D, Chern G, Mathias H and Testardi L R 1992 *Phys. Rev.* B **45** 1838
[32] Camley R E 1987 *Phys. Rev.* B **35** 3608
[33] Camley R E and Tilley D R 1988 *Phys. Rev.* B **37** 3413
[34] Camley R E 1989 *Phys. Rev.* B **39** 12316
[35] Dieny B, Gavigan J P 1990 *J. Phys.: Condens. Matter* **2** 187
Dieny B, Gavigan J P and Rebouillet J P 1990 *J. Phys.: Condens. Matter* **3** 159
[36] Larsen C C, Jensen J and Mackintosh A R 1987 *Phys. Rev. Lett.* **49** 712
Bohr J, Gibbs D, Axe J D, Moncton D E, D'Amico K L, Majkrzak C F, Kwo J, Hong M, Chien C L and Jensen J 1989 *Physica* B **159** 93
[37] Xuan-Zhang Wang 1991 *Phys. Lett.* **154A** 425
Xuan-Zhang Wang, Yun-Cheng Ge and Zhan Zhang 1991 *J. Phys.: Condens. Matter* **3** 5107
[38] Carriço A S and Camley R E 1992 *Phys. Rev.* B **45** 13117; *Solid State Commun.* **82** 161
[39] Hinchey L L and Mills D L 1986 *Phys. Rev.* B **33** 3329; **34** 1689
[40] Wang R W and Mills D L 1992 *Phys. Rev.* B **46** 11681
[41] Schwenk D, Fishman F and Schwabl F 1988 *Phys. Rev.* B **38** 11618
[42] Sy H K and Ow M H 1992 *J. Phys.: Condens. Matter* **4** 5891
[43] Some previous presentations did not give the expression for the total free energy correctly. The numerical results however are correct.
[44] Corciovei A, Costache G and Vamanu D 1972 *Solid State Physics* vol 27, ed H Ehrenreich, F Seitz and D Turnbull (New York: Academic) p 237
[45] Yafet Y 1987 *J. Appl. Phys.* **61** 4058
[46] Yafet Y, Kwo J, Hong M, Majkrzak C F and O'Brien T 1988 *J. Appl. Phys.* **63** 3453
[47] Parkin S S P 1991 *Phys. Rev. Lett.* **67** 3598
[48] Parkin S S P, Li Z G and Smith D J 1991 *Appl. Phys. Lett.* **54** 2170
[49] Wang Y, Levy P M and Fry J L 1990 *Phys. Rev. Lett.* **65** 2732
[50] Edwards D M, Mathon J and Muniz R B and Phan M S 1991 *J. Phys.: Condens. Matter* **3** 4941
[51] Mathon J, Villeret M and Edwards D M 1992 *J. Phys.: Condens. Matter* **4** 9873
[52] Barnas J 1992 *J. Magn. Magn. Mater.* **111** L215
[53] Bruno P and Chappert C 1991 *Phys. Rev. Lett.* **67** 1602
[54] The results presented here are equivalent to those found in [37].
[55] Takanashi K, Kamiguchi Y, Fujimori H and Motokawa M 1992 *J. Phys. Soc. Japan* **61** 3721
[56] Dufour C, Bauer Ph, Sajieddine M, Cherifi K, Marchal G, Mangin Ph and Camley R E 1993 *J. Magn. Magn. Mater.* at press
[57] Elliot R J 1966 *Magnetism* vol 11A, ed G Rado and H Suhl (New York: Academic) p 385
[58] Hong M, Flemming R M, Kwo J, Schneemyer L F, Waszczak J V, Mannaerts J P, Majkrzak C F, Gibbs D and Bohr J 1987 *J. Appl. Phys.* **61** 4054
[59] LePage J G and Camley R E 1990 *Phys. Rev. Lett.* **65** 1152
[60] Nörtemann F C, Stamps R L, Carriço A S and Camley R E 1992 *Phys. Rev.* B **46** 10847
[61] Motokawa M 1991 *Prog. Theor. Phys. Suppl.* **101** 537; *J. Phys. Soc. Japan* **60** 1355
[62] Yuan Jian 1989 *J. Phys.: Condens. Matter* **1** 7951
[63] Wang Xuan-Zhang and Zhang Zhan 1990 *J. Phys.: Condens. Matter* **2** 5765

[64] Prigge S, Roux H and Bauer E 1981 *Surf. Sci.* **107**
Rau C, Jin C and Robert M 1988 *J. Appl. Phys.* **63** 3667
[65] Siegman H C, Mauri D, Scholl D and Kay E 1988 *J. Physique Coll.* **49** C8 9
[66] Cottam M G, Slavin A (ed) 1993 *Spin Waves and Nonlinear Excitations in Magnetic Thin Films and Superlattices* (Singapore: World Scientific)
[67] Cottam M G and Lockwood D J 1986 *Light Scattering in Magnetic Solids* (Toronto: Wiley)
[68] Grünberg P 1989 *Light Scattering in Solids V* ed M Cardona and G Güntherodt (Berlin: Springer)
Patton C E 1984 *Phys. Rep.* **103** 251
[69] Hillebrands B and Güntherodt G 1993 *Ultrathin Magnetic Structures II* ed J A C Bland and B Heinrich (Berlin: Springer)
See also the article by J R Dutcher in [66].
[70] Grimsditch M 1989 *Light Scattering in Solids V* ed M Cardona and G Güntherodt (Berlin: Springer)
[71] Borovik-Romanov A S and Kreines N M 1988 *Spin Waves and Magnetic Excitations* ed A S Borovik-Romanov and S K Sinha (Amsterdam: Elsevier)
[72] Bland J A C, Johnson A D, Lauter H J, Bateson R D, Blundell S J, Shackleton C and Penfold J 1991 *J. Magn. Magn. Mater.* **93** 513
[73] Collins M F 1989 *Magnetic Critical Scattering* (Oxford: Oxford University Press)
[74] Sanders R W, Belanger R M, Motokawa M and Jaccarino V 1981 *Phys. Rev.* B **23** 1190
[75] Remer L, Lüthi B, Sauer H, Beick R and Camley R E 1986 *Phys. Rev. Lett.* **56** 2752
[76] Oliveros M C, Almeida N S, Tilley D R, Thomas J and Camley R E 1992 *J. Phys.: Condens. Matter* **4** 8497
Camley R E, Cottam M G and Tilley D R 1992 *Solid State Commun.* **81** 571
[77] Cottam M G and Tilley D R 1989 *Introduction to Surface and Superlattice Excitations* (Cambridge: Cambridge University Press)
[78] Hillebrands B, Baumgart P, Mock R and Güntherodt G 1986 *Phys. Rev.* B **34** 9000
[79] Maradudin A A and Mills D L 1967 *J. Phys. Chem. Solids* **28** 1855; erratum 1969, *J. Phys. Chem. Solids* **30** 784
[80] Levy J C S 1981 *Surf. Sci. Rep.* **1** 39
[81] Mathon J 1988 *Rep. Prog. Phys.* **51** 1
[82] Diep H T 1991 *Phys. Rev.* B **43** 8509
[83] Stamps R L, Harzer J V and Hillebrands B 1992 *J. Magn. Magn. Mater.* **104–7** 1868
[84] Martinez B and Camley R E 1992 *J. Phys. C: Solid State Phys.* **4** 5001
[85] Erickson R P and Mills D L 1992 *Phys. Rev.* B **46** 861
[86] Rahman T S and Mills D L 1979 *Phys. Rev.* B **20** 1173
[87] Kalinikos B A, Kovshikov N G and Slavin A N 1988 *Sov. Phys.–JETP* **67** 303 (1988 *Zh. Eksp. Teor. Fiz.* **94** 159)
[88] Almeida N S and Mills D L 1987 *Phys. Rev.* B **36** 2015
Kahn L, Almeida N S and Mills D L 1988 *Phys. Rev.* B **37** 8072
[89] Kronig R de L and Penney W G 1930 *Proc. R. Soc.* A **130** 499
[90] Morrish A H 1983 *The Physical Principles of Magnetism* (Malabar, FL: Kreiger)
[91] Walker L R 1957 *Phys. Rev.* **105** 390
[92] Damon R W and Eshbach J R 1961 *J. Phys. Chem. Solids* **19** 308
[93] Albuqurque E L, Fulco P and Tilley D R 1986 *Rev. Bras. Fis.* **16** 315
[94] Barnas J 1988 *J. Phys. C: Solid State Phys.* **21** 1021
[95] Camley R E 1987 *Surf. Sci. Rep.* **7** 103
[96] Nörtemann F C, Stamps R L and Camley R E 1993 *Phys. Rev.* B at press
[97] Vecris G and Quinn J L 1991 *Phys. Rev.* B **43** 8303
[98] Nörtemann F C, Stamps R L, Camley R E, Hillebrands B and Güntherodt G 1993 *Phys. Rev.* B **47** 3225
[99] Agranovich V M and Kratsov V E 1985 *Solid State Commun.* **55** 85
[100] Almeida N S and Mills D L 1988 *Phys. Rev.* B **37** 3400
[101] Raj N and Tilley D R 1987 *Phys. Rev.* B **36** 7003
[102] Stamps R L, Camley R E, Nörtemann F C and Tilley D R 1993 unpublished
[103] Almeida N S and Tilley D R 1990 *Solid State Commun.* **73** 23
[104] Cottam M G, Camley R E and Tilley D R 1992 *Solid State Commun.* **55** 85
[105] Almeida N S and Tilley D R 1991 *Phys. Rev.* B **43** 11 145
[106] Faßbender J, Nörtemann F C, Stamps R L, Camley R E, Hillebrands B, Güntherodt G and Parkin S S P 1992 *Phys. Rev.* B **46** 5810
[107] Faßbender J 1992 *Diplomarbeit* RWTH-Aachen
[108] Wolfram T and Dewames R E 1972 *Prog. Surf. Sci.* **2** 233

[109] Hillebrands B 1990 *Phys. Rev.* B **41** 530
Experimental verification of 'exchange modes' in superlattices can be found in Hillebrands B, Harzer J V, Güntherodt G, England C D and Falco C M 1990 *Phys. Rev.* B **42** 6839
[110] Vohl M, Barnas J and Grünberg P 1989 *Phys. Rev.* B **39** 12003
Demokritov S, Wolff J A and Grünberg P 1991 *Europhys. Lett.* **15** 881
[111] Hoffmann F 1970 *Phys. Status Solidi* **41** 807
[112] Barnas J 1991 *J. Magn. Magn. Mater.* **102** 319
[113] Mills D L 1992 *Phys. Rev.* B **45** 13 100
[114] Benson H and Mills D L 1968 *Phys. Rev.* B **178** 839
[115] s_{tran} is defined as $[|s_x|^2 + |s_y|^2]^{1/2}$. Care must be taken when calculating the magnitudes $|s_x|^2$ and $|s_y|^2$ however, since the equation of motion matrix is non-Hermitian. This means appropriate right and left eigenvectors must be used. See [96].
[116] Binasch G, Grünberg P, Saurenbach F and Zinn W 1989 *Phys. Rev.* B **39** 4828
[117] Baibich M N, Broto J M, Fert A, Van Dau F Nguyen, Petroff F, Etienne P, Creuzet P, Friederich A and Chazelas J 1988 *Phys. Rev. Lett.* **61** 2472
[118] Rodmacq B, George B, Vazzadeh M and Mangin Ph 1992 *Phys. Rev.* B **46** 1206
[119] Vélu E, Dupas C, Renard D, Renard J P and Seiden J 1988 *Phys. Rev.* B **37** 668
[120] McGuire T R and Potter R I 1975 *IEEE Trans. Magn.* **MAG-11** 1018
[121] Krebs J, Lubitz P, Chaiken A and Prinz G A 1989 *Phys. Rev. Lett.* **63** 1645
Chaiken A, Prinz G A and Krebs J 1990 *J. Appl. Phys.* **87** 4892
[122] Pratt W P, Lee S F, Slaughter M, Loloee R, Schroeder P A and Bass J 1991 *Phys. Rev. Lett.* **66** 3036
[123] Zhang S and Levy P M 1991 *J. Appl. Phys.* **69** 4768
[124] Fert A and Campbell I A 1976 *J. Phys. F: Met. Phys.* **6** 849
Jaoul O, Campbell I A and Fert A 1977 *J. Magn. Magn. Mater.* **5** 23
Campbell I A and Fert A 1982 *Ferromagnetic Materials* vol 3, ed E P Wohlfarth (Amsterdam: North-Holland) p 747
[125] Camley R E and Barnas J 1989 *Phys. Rev. Lett.* **63** 664
[126] Barnas J, Fuss A, Camley R E, Grünberg P and Zinn W 1990 *Phys. Rev.* B **42** 8110
[127] Johnson B L and Camley R E 1991 *Phys. Rev.* B **44** 9997
[128] Fuchs K 1938 *Cambridge Phil. Soc.* **34** 100
Sondheimer H 1952 *Adv. Phys.* **1** 1
[129] Hood R Q and Falicov L M 1992 *Phys. Rev.* B **46** 8287
[130] Barthelemy A and Fert A 1991 *Phys. Rev.* B **43** 13 124
[131] Tesanovic Z, Jaric M V and Maekawa S 1986 *Phys. Rev. Lett.* **57** 2760
[132] Levy P M, Zhang S and Fert A 1990 *Phys. Rev. Lett.* **65** 1643
[133] Levy P M, Ounadjela K, Zhang S, Wang Y, Sommers C B and Fert A 1990 *J. Appl. Phys.* **67** 5914
[134] Dieny B 1992 *Europhys. Lett.* **17** 261
Dieny B, Speriosu V S, Nozieres J P, Gurney B A, Vedyayev A and Ryzhanova N 1992 *NATO Advanced Research Workshop on Structure and Magnetic Properties of Systems in Reduced Dimension* ed R Farrow, B Dieny, A Fert, M Donath and B Hershier (New York: Plenum) at press
[135] Vedyayev A, Dieny B and Ryzhanova N 1992 *Europhys. Lett.* **19** 329
Dieny B, Meyer H, Vedyayev A and Ryzhanova N 1992 *Proc. E-MRS (Lyon)* at press
[136] Camblong H E and Levy P M 1992 *Phys. Rev. Lett.* **69** 2835
[137] Edwards D M, Mathon J and Muniz R B 1991 *IEEE Trans. Magn.* **MAG-27** 3548
[138] Parkin S S P 1992 *Appl. Phys. Lett.* **61** 1358
[139] Fullerton E E, Kelly D M, Guimpel J, Schuller I K and Bruynseraede Y 1992 *Phys. Rev. Lett.* **68** 859
[140] Joo S, Obi Y and Takanashi K 1992 *J. Magn. Magn. Mater.* **104–7** 1753
[141] Huang T C, Nozieres J P and Speriosu V S 1992 *Appl. Phys. Lett.* **60** 1573
[142] Obi Y, Takanashi K and Mitani Y 1992 *J. Magn. Magn. Mater.* **104–7** 1747
[143] Baumgart P, Gurney B A, Wilhoit D R, Nguyen T, Dieny B and Speriosu V S 1991 *J. Appl. Phys.* **69** 4792
Gurney B A, Baumgart P, Wilhoit D R, Dieny B and Speriosu V S 1991 *J. Appl. Phys.* **70** 5867
[144] Takanashi K, Obi Y, Tsuda N and Fujimori H 1992 *J. Phys. Soc. Japan* **61** 4148
[145] Barnas J, Fuss A, Camley R E, Walz U, Grünberg P and Zinn W 1990 *Vacuum* **41** 1241
[146] Doughton J M, Bade P A and Jenson M L 1992 *IEEE Trans. Magn.* **MAG-28** 2488
[147] Dieny B, Speriosu V S, Metin S, Parkin S S P, Gurney B A, Baumgart P and Wilhoit D R 1991 *J. Appl. Phys.* **69** 4774
[148] Dieny B, Speriosu V S, Parkin S S P, Gurney B A, Wilhoit D R and Mauri D 1991 *Phys. Rev.* B **43** 1297
[149] Inoue J, Oguri A and Maekawa S 1992 *J. Magn. Magn. Mater.* **104–107** 1883

[150] Inoue J and Maekawa S 1991 *Prog. Theor. Phys.* **106** 187
[151] Okiji A, Nakanishi H, Sakata K and Kasai H 1992 *Japan. J. Appl. Phys.* **31** L706
[152] Hasegawa H 1992 *J. Phys.: Condens. Matter* **4** 169; 1992 Preprint
[153] Oguri A, Asano Y and Maekawa S 1992 *J. Phys. Soc. Japan* **61** 2652
[154] Jiang S J 1992 *Appl. Phys. Lett.* **61** 2362
[155] Xiao J Q, Jiang S J and Chien C L 1992 *Phys. Rev.* B **46** 9266
[156] Xiao J Q, Jiang S J and Chien C L 1991 *Phys. Rev. Lett.* **68** 3749
[157] Berkowitz A E, Mitchell J R, Carey M J, Young A P, Zhang S, Spada F E, Parker F T, Hutten A and Thomas G 1992 *Phys. Rev. Lett.* **68** 3745
[158] Zhang Shufeng 1992 *Appl. Phys. Lett.* **61** 1855
[159] Mathon J 1988 *Rep. Prog. Phys.* **51** 1
[160] Falicov L M, Pierce D T, Bader S D, Gronsky R, Hathaway Kristl B, Hopster H J, Lambeth D N, Parkin S S P, Prinz G, Salamon M, Schuller I K and Victora R H 1990 *J. Mater. Res.* **5** 1299
[161] Lee J I, Fu C L and Freeman A J 1986 *J. Magn. Magn. Mater.* **62** 93
[162] den Broeder F J A, Hoving W and Bloemen P J H 1991 *J. Magn. Magn. Mater.* **93** 562
[163] Lee C H, He Hui, Lamelas F J, Vavra W, Uher C and Clarke R 1990 *Phys. Rev.* B **42** 1066
[164] Borchers J A, Salamon M B, Erwin R W, Rhynne J J, Du R R and Flynn C P 1991 *Phys. Rev.* B **43** 3123
[165] Erickson R P and Mills D L 1992 *Phys. Rev.* B **46** 861
Pescia D and Pokrovsky V L 1990 *Phys. Rev. Lett.* **65** 2599
[166] Dutcher J R, Cochran J F, Jacob I and Egelhoff W G Jr 1989 *Phys. Rev.* B **39** 10430
Pappas D P, Kämper P and Hopster H 1990 *Phys. Rev. Lett.* **64** 3179
[167] Pant Bharat B 1987 *Sci. Honeyweller* **8** 29
[168] Mee C D and Daniel E D (ed) *Magnetic Recording I: Technology* (New York: McGraw-Hill)
[169] Pohm A V, Comstock C S and Daughton J M 1990 *IEEE Trans. Magn.* **MAG-25** 4266
[170] de Wit H J 1992 *Rep. Prog. Phys.* **55** 113
[171] Weller D and Reim W 1989 *Appl. Phys.* A **49** 59
[172] Stamps R L and Hillebrands B 1991 *J. Magn. Magn. Mater.* **93** 616